Correction 08/21/20

The potential for aqueous fluid-rock and silicate melt-rock interactions to re-equilibrate hydrogen in peridotite nominally anhydrous minerals

Kendra J. Lynn* and Jessica M. Warren

University of Delaware
Department of Earth Sciences
255 Academy St, 103 Penny Hall
Newark, DE 19716 USA

*corresponding author
E-mail: kjlynn@udel.edu

Running title: Timescales of H re-equilibration in peridotite NAMs
Keywords: nominally anhydrous minerals, peridotite, diffusion, hydrogen

Abstract

Hydrogen is a rapidly diffusing monovalent cation in nominally anhydrous minerals (NAMs, such as olivine, orthopyroxene, and clinopyroxene), which is potentially re-equilibrated during silicate melt-rock and aqueous fluid-rock interactions in massif and abyssal peridotites. We apply a 3D numerical diffusion modeling technique to provide first-order timescales of complete hydrogen re-equilibration in olivine, clinopyroxene, and orthopyroxene over the temperature range 600-1200°C. Model crystals are 1-3 mm along the c-axis and utilize H^+ diffusion coefficients appropriate for Fe-bearing systems. Two sets of models were run with different boundary compositions: 1) "low-H models" are constrained by mineral-melt equilibrium partitioning with a basaltic melt that has 0.75 wt% H_2O and 2) "high-H models," which utilize the upper end of the estimated range of mantle water solubility for each phase. Both sets of models yield re-equilibration timescales that are identical and are fast for all phases at a given temperature. These timescales have strong log-linear trends as a function of temperature (R^2 from 0.97 to 0.99) that can be used to calculate expected re-equilibration time at a given temperature and grain size. At the high end of the model temperatures (1000-1200°C), H^+ completely re-equilibrates in olivine, orthopyroxene, and clinopyroxene within minutes to hours, consistent with previous studies. These short timescales indicate that xenolith NAM mantle water contents are likely to be overprinted prior to eruption. The models also resolve the decoupled water-trace element relationship in Southwest Indian Ridge peridotites, in which peridotite REE abundances are reproduced by partial melting models whereas the relatively high NAM H_2O contents require later re-equilibration with melt.

At temperatures of 600-800°C, which correspond to conditions of hydrothermal alteration of pyroxene to amphibole and talc, H^+ re-equilibration typically occurs over a range of timescales spanning days to years. These durations are well within existing estimates for the duration of fluid flow in oceanic hydrothermal systems, suggesting that peridotite NAM water contents are susceptible to diffusive overprinting during higher temperature hydrothermal alteration. Thus, diffusion during aqueous fluid-rock interactions may also explain NAM H_2O contents that are too high to reflect residues of melting. These relatively short timescales at low temperatures suggest that the origin of water contents measured in peridotite NAMs requires additional constraints on sample petrogenesis, including petrographic and trace element analyses. Our 3D model results also hint that H^+ may diffuse appreciably during peridotite serpentinization, but diffusion coefficients at low temperature are unconstrained and additional experimental investigations are needed.

Introduction

The water contents of olivine, orthopyroxene, and clinopyroxene in peridotites have been used to constrain the water content of the upper mantle, a value that is important for many mantle properties, including melting depth and viscosity (e.g., Mackwell et al. 1985; Hirth and Kohlstedt 1996; Ingrin and Skogby 2000; Peslier 2010). The hydrogen incorporated in these nominally anhydrous minerals (NAMs) is sometimes referred to as "water" or "hydroxyl" because of its chemical bond with oxygen within the olivine structure, but here we refer to this species as hydrogen or H^+. Hydrogen is a rapidly diffusing monovalent cation (Figure 1) and its re-equilibration in response to silicate melt-rock interactions quickly modifies NAM water contents (e.g., Mackwell and Kohlstedt 1990; Kohlstedt and Mackwell 1998; Ingrin and Skogby 2000; Stalder and Skogby 2003; Ingrin and Blanchard 2006).

Thermally driven diffusion in igneous minerals is now widely used to quantify the timescales of geologic processes operating in diverse tectonic settings (e.g., Costa and Dungan 2005; Shea et al. 2015a; Ruth et al. 2018). Hydrogen diffusion chronometry has classically been applied at high temperatures (e.g., 1000-1200°C), where it records short-lived processes such as magma ascent (Demouchy et al. 2006; Peslier and Luhr 2006; Denis et al. 2015; Lloyd et al. 2016) and melt inclusion re-equilibration during degassing/decompression of melts (e.g., Le Voyer et al. 2014). Yet it has the strong potential to be applied to lower temperature geologic processes such as hydrothermal fluid-rock interactions, which can occur at temperatures up to 1000°C (e.g., Fumagalli et al. 2009). In addition, the timescales of H^+ re-equilibration in NAMs at temperatures <1000°C need to be re-evaluated in light of recent advances in diffusion modeling techniques and experimentally determined diffusion rates.

In this study, we evaluate first order timescales of complete hydrogen re-equilibration over a temperature range of 600-1200°C. Models at 1200°C allow us to compare our results with previous studies and to consider re-equilibration timescales for NAMs in peridotite xenoliths. We use models at 800-1200°C to evaluate silicate melt-rock interactions and models at 600-800°C to evaluate the circulation of high temperature (high-T) hydrothermal fluids in peridotites. Our objective is to constrain the likely kinetic window of H^+ (i.e., time required for complete re-equilibration) to evaluate the potential for H chronometry to be used in natural samples for assessing the timescales over which aqueous fluids and silicate melts interact with the mantle.

Modeling Methodology

Diffusion chronometry in igneous minerals is typically used to evaluate timescales of high-temperature (>800°C) processes in magmatic systems. Below 800°C, appreciable diffusion no longer occurs for most elements in silicate minerals (e.g., Fe-Mg in olivine; Dohmen and Chakraborty 2007a, 2007b). However, projected H^+ diffusion coefficients (D_H) in NAMs at 600°C (10^{-13} to 10^{-15} m^2/s; Figures 1 and 2) may be faster than Fe-Mg diffusion in olivine at 1200°C (cf. $D_{Fe\text{-}Mg} = 10^{-16}$ m^2/s, for Fo_{90} olivine using a simplified Arrhenius form of D_{FeMg}). This latter chronometer is routinely used to investigate timescales of weeks to years in magmatic systems (e.g., Costa and Dungan 2005; Kahl et al. 2011; Lynn et al. 2017a, 2017b; Viccaro et al. 2019), suggesting that H^+ diffusion could be re-equilibrating NAM water contents over similar timescales. Thus, even at relatively low temperatures of 600°C, hot hydrothermal fluids and/or partial melts could significantly modify peridotite NAM water contents over geologically reasonable timescales.

To constrain the possible timescales of H^+ re-equilibration during silicate melt-rock and aqueous fluid-rock interactions, we used 3D numerical models of H^+ diffusion in single crystals of olivine, orthopyroxene, and clinopyroxene. Below we outline our (i) 3D modeling rationale, (ii) choice of diffusion coefficients for each mineral phase, (iii) numerical model setup, and (iv) method to account for uncertainties.

Three-dimensional modeling rationale

Hydrogen diffusion in NAMs has typically been investigated by modeling one-dimensional traverses across a two-dimensional crystal section (e.g., Demouchy and Mackwell 2006; Demouchy et al. 2006; Gose et al. 2011; Tian et al. 2017). However, crystals are three-dimensional objects with complex geometries and diffusive re-equilibration often occurs at different rates along the principle crystallographic axes of silicate minerals (i.e., diffusion anisotropy; Zhang 2010). Three-dimensional volume diffusion of H^+ in sphere and cube geometries was explored by Thoraval and Demouchy (2014), who showed that a 3D approach is needed to accurately account for highly anisotropic diffusing species (i.e., >2x difference in diffusion coefficients along different axes). Shea et al. (2015b) subsequently showed that sphere and cube geometries are insufficient to capture sample variability, so we utilize 3D euhedral morphologies that better represent natural samples, account for anisotropy, and address complexities that arise from off-center and oblique sectioning (see Supplementary Material for more details).

Natural peridotites have a range of grain sizes and crystal shapes (Boullier and Nicholas 1975; Mercier and Nicolas 1975; Tabor et al. 2010; Achenbach et al. 2011) complicating the choice of crystal shape in the models. One option to describe peridotite crystal morphologies is a tetrakaidecahedron (Hiraga et al. 2007), which allows minimal surface area and maximizes the packing of equal-sized, similarly shaped objects. However, natural peridotites can exhibit variations in grain size and shape that are not represented well by tetrakaidecahedrons (Tabor et al. 2010). Here, pyroxene and olivine models are built with cube-shaped voxels (a pixel in 3D) into euhedral crystal morphologies with relatively equant aspect ratios for simplicity (Figure 3). The olivine model geometry is adapted from Shea et al. (2015b) and Lynn et al. (2017b). Pyroxene models are modified after Krimer and Costa (2017) and Jollands and Müntener (2019).

Choice of Diffusion Coefficients

The major, minor, and trace element chemistry of NAMs can have a significant effect on hydrogen incorporation and on subsequent diffusion. Diffusion experiments that have utilized pure mineral endmembers, synthetic, and/or doped starting materials have identified several diffusion mechanisms that are significantly affected by crystal chemistry (e.g., Mosenfelder et al.

2006; Padrón-Navarta et al. 2014; Jollands et al. 2016; Faul et al. 2016; Tollan et al. 2018). However, several studies using natural olivine and pyroxene crystals (that are not compositional end-members) yield distinctly different results with important implications for diffusion in natural systems (Woods et al. 2010; Ferriss et al. 2016, 2018; Thoraval et al. 2018; Jollands et al. 2019; Barth et al. 2019). This suggests that the compositional complexities of natural minerals significantly influence the mechanisms by which hydrogen moves through a crystal.

Vacancies associated with Si have the slowest diffusion coefficients (Padrón-Navarta et al. 2014) and can also play an important role in H^+ incorporation and diffusion at high pressure and temperature conditions (e.g., Mosenfelder et al. 2006; Demouchy et al. 2016; Padrón-Navarta and Hermann 2017), low silica activity (Lemaire et al. 2004; Costa and Chakraborty 2008), and high water activity (Tollan et al. 2017). However, the slow $D_{H[Si]}$ that Padrón-Navarta et al. (2014) measured in a synthetic Fe-free forsterite probably reflects the slow diffusion of Si (Costa and Chakraborty 2008). Similar experiments conducted on natural olivine samples show instead that inter-site redistribution of H^+ from the Si site allows fast removal of H^+ via the proton-polaron or proton-vacancy mechanisms (Jollands et al. 2019). The [Si] diffusion mechanism likely does not affect the first-order diffusion rates that we obtain with our models here, even though it may be important during crystal growth or at high pressures in subduction zones (e.g., Kempf and Hermann 2018; Jollands et al. 2019). Thus, the following selection of D_H values is based primarily on the presence of Fe (Mackwell and Kohlstedt 1990; Demouchy and Mackwell 2006; Woods et al. 2000; Stalder and Skogby 2003; Ferriss et al. 2016; Ferriss et al. 2018).

Hydrogen diffusion in olivine has typically been modeled using one of two distinct diffusion behaviors. The faster diffusion of H^+ is attributed to a flux of hydrogen (i.e., protons) charge balanced by a flux of electrons from Fe^{2+} to Fe^{3+}. The flux of electron holes associated with Fe^{3+}, often referred to as polarons, give rise to the name “proton-polaron” or “redox” mechanism when describing this type of diffusion (Mackwell and Kohlstedt 1990). The second behavior is characterized by slower diffusion associated with metal vacancies in the crystal lattice and is referred to as the “proton-vacancy” mechanism (e.g., Demouchy and Mackwell 2006). Most applications of hydrogen diffusion chronometry have used either the fast proton-polaron or the slower proton-vacancy mechanism to explain H^+ mobility (e.g., Demouchy et al. 2006; Peslier and Luhr 2006).

Here we focus on the hydration of NAMs, in contrast to many previous applications of H^+ diffusion chronometry, which have mainly focused on dehydration (e.g., degassing in magmatic systems). The extensive experimental datasets for olivine (e.g., Mackwell and Kohlstedt 1990; Kohlstedt and Mackwell 1998; Demouchy and Mackwell 2006; Jollands et al. 2016; Ferriss et al. 2018) suggest that the absolute rates of each diffusion mechanism do not vary but rather that different mechanisms might dominate during the course of re-equilibration. Although H^+ diffusion appears initially to be dominated by the fast proton-polaron mechanism before it transitions to the slower vacancy mechanism (Thoraval and Demouchy 2014; Ferriss et al. 2018), this switch in behavior is mostly relevant when extracting short (e.g., minutes) timescales of eruptive processes. For the longer time-scale processes of melt-rock and fluid-rock interaction in mantle rocks, the proton-polaron and vacancy mechanisms are considered independent processes during hydration and these likely bracket the possible timescales of H re-equilibration, as suggested by Thoraval and Demouchy (2014). In addition, recent dehydration experiments using natural olivine suggest that H^+ diffusion may be modeled with a rate intermediate between the fast proton-polaron mechanism and the slower vacancy mechanism (Ferriss et al. 2018).

We thus ran three sets of models for olivine, utilizing (i) the total H^+ diffusion rate from dehydration experiments (Ferriss et al. 2018; Figure 1), (ii) the proton-polaron mechanism (Mackwell and Kohlstedt 1990), (iii) and the proton-vacancy mechanism (Demouchy and Mackwell 2006). Diffusion coefficients are summarized in Supplementary Table S1. Diffusion is fastest along the *a*-axis for the total H+ diffusion rate and the proton-polaron mechanism, but fastest along the *c*-axis for the proton-vacancy mechanism. We also assume that the mobility of H^+ in the natural NAMs that are the focus of this study are not subject to inter-site reaction limited diffusion constraints as proposed by Jollands et al. (2019), meaning that H^+ is not restricted to the slowest diffusing [Si] mechanism.

For pyroxene, our models (Table S1) utilize H^+ diffusion coefficients for Fe-bearing clinopyroxene (cpx) and orthopyroxene (opx) as mantle pyroxenes are Fe-bearing. These coefficients have been shown to be faster than in low-Fe or Fe-free compositions (e.g., Woods et al. 2000; Stalder and Skogby 2003; Ferriss et al. 2016; Yang et al. 2019). Clinopyroxene models were run with the anisotropic Fe-bearing diffusion rates from Jaipur diopside (Woods et al. 2000; Ferriss et al. 2016). Jaipur has a composition different from peridotite diopside, but is the best available diffusion data for Fe-bearing cpx. Orthopyroxene models utilize Fe-bearing diffusion rates from Kilbourne Hole opx experiments, which provide an Arrhenius relationship for [001] (Stalder and Skogby 2003; Bell et al. 1995). Stalder and Skogby (2003) showed that diffusion along [010] is about one order of magnitude slower than [001] and that [100] is intermediate between these two at 700°C. The Arrhenius relationship cannot be calculated for the [100] and [010] axes due to limited experiments at different temperatures. Thus, our 3D models and error envelopes use the Arrhenius relationship for [001] only (e.g., as if opx were isotropic), so our model results are likely minimum timescales of complete opx re-equilibration.

These Fe-bearing pyroxene diffusion coefficients likely represent the proton-polaron mechanism, which may be a factor of 3x faster than the vacancy mechanism, based on constraints available for olivine mechanisms (Ingrin and Blanchard, 2006). To evaluate the potential role of a slower diffusion mechanism in pyroxene, we ran additional models using the vacancy diffusion rate of Sundvall et al. (2009) for diopside and Stalder and Behrens (2006) for enstatite. These models provide examples of possible slower vacancy-controlled diffusion timescales, which might dominate H^+ mobility over the longer timescales of silicate melt-rock and aqueous fluid-rock interactions.

Model Setup

Our models are based on previous 3D diffusion approaches (see Shea et al. 2015; Lynn et al. 2017; Jollands and Müntener 2019). Details of the numerical implementation of the models and their equations are given in the Supplementary Material. Initial conditions (i.e., starting NAM water contents) were selected based on the low end of the estimated water concentration range for bulk upper mantle (e.g., Hirschmann 2006). The lower value of 50 ppm H_2O in the bulk mantle (Hirschmann 2006), combined with estimates for upper mantle mineral modes (Workman and Hart 2005), was used to set initial conditions to 7 ppm H_2O in olivine, 50 ppm H_2O in opx, and 200 ppm H_2O in cpx. All phases were initially homogeneous prior to the onset of diffusion. Several sets of boundary conditions were used to simulate the high end of the range for bulk upper mantle (Table 1) and conditions appropriate for hydrothermal fluid-rock interactions (see Supplementary Material for details).

Models were run with D_H values calculated at 600°C, 700°C, 800°C, 1000°C, and 1200°C using the experimentally determined Arrhenius relationships (compiled in the Supplementary Data File, Table S1). Our extrapolation of the Arrhenius relationships for hydrogen diffusivities extend 100-200°C beyond the experimentally constrained range (Figures 1 and 2 in the main text) and we also model uncertainties associated with extrapolation of the experimental datasets (discussed in detail below). Pyroxene vacancy models (Stalder and Behrens, 2006 for opx; Sundvall et al. 2009 for cpx) were run at 600°C, 800°C, and 1000°C where the slower mechanism might dominate diffusion behavior.

After diffusion simulations were completed, the 3D numerical crystals were sectioned through their cores perpendicular to the *c*-axis (an *a*-*b* section; Figure 3). The area of this section is ~0.9 mm^2 for the 1 mm models and 2.4 mm^2 for the 3 mm models, well within the range of mean grain areas for the textures typically observed in peridotites (e.g., Tabor et al. 2010; Achenbach et al. 2011). The concentration of the central pixel in the 2D section (Figure 3) is sampled at regular model time intervals to track changes in core water content (after Thoraval and Demouchy 2014). Model results are reported as % re-equilibration, allowing all NAM phases to be compared despite different absolute water contents (after Costa et al. 2003; Lynn et al. 2017b). The % re-equilibration represents the change in concentration between the initial H^+ content and the "measured" (e.g., diffused) H^+ after a given diffusion duration:

$$\text{\% re-equilibration}=\frac{H_{\text{initial}}-H_{\text{measured}}}{H_{\text{initial}}-H_{\text{equilibrium}}}\times 100 \qquad (1)$$

where $H_{initial}$ is the initial water content before diffusion, $H_{measured}$ is the core composition sampled at various time intervals throughout the diffusion model, and $H_{equilibrium}$ is the boundary condition assigned to the model (Table 1).

Accounting for Uncertainties

A key component of evaluating model applications to natural samples is a thorough consideration of associated uncertainties. Our approach seeks to broadly constrain the timescales of complete H re-equilibration in peridotite NAMs rather than provide unique solutions to individual mineral profiles. Therefore, we treat timescale uncertainties by evaluating the 95% confidence interval on experimental diffusion data (e.g., error envelopes), variations due to differences in mineral grain size, random sectioning of natural samples (Shea et al. 2015b), and fundamental environmental parameters that diffusion models are sensitive to (e.g., temperature, compositional boundary conditions). Models were run using predicted diffusion coefficients calculated from Arrhenius relationships at a given temperature, along with two additional models at each temperature representing the upper and lower bounds of uncertainty in the experimental diffusion coefficients (see Supplementary Table S2). The 1 and 3 mm models encompass most of the range of grain sizes in natural peridotites (Tabor et al. 2010). To account for uncertainties in grain orientations and sectioning of natural peridotite samples, we randomly sliced a 3D opx model 200 times and "measured" the H content at the core of each section (after Lynn et al. 2017b). This provides the distribution of NAM water contents expected in a given peridotite sample subject to 2D sectioning effects. Finally, we tested different boundary conditions reflecting a range of environmental conditions that drive diffusion (Table 1).

Results

A total of 214 models were run to constrain the kinetic window of H^+ in NAMs. In the first set of 100 models orthopyroxene, clinopyroxene, and three olivine diffusion mechanisms were run for each set of silicate melt boundary conditions (low-H vs. high-H models), both grain sizes (1 and

3 mm) and five temperature intervals (40 pyroxene and 60 olivine models in total). No differences in 100% re-equilibration timescale were observed between the two sets of boundary conditions, indicating that the complete re-equilibration of NAMs is mainly sensitive to the diffusion coefficient. An additional two models that tested hydrothermal boundary conditions (10^3 and 10^4 ppm) for 1 mm cpx at 800ºC have the same 100% re-equilibration timescales as the low-H and high-H silicate melt cpx models (boundary conditions of 353 and 750 ppm, respectively) at the same temperature. This confirms that the 100% re-equilibration timescales are insensitive to changes in boundary conditions, due to the current set of experimentally determined Arrhenius laws being non-concentration dependent.

Modeled re-equilibration timescales for each mineral (filled symbols in Figure 4) have strong log-linear trends of 100% re-equilibration time as a function of temperature with R^2 values 0.97-0.99. The re-equilibration of H^+ in all phases is fast at 1200°C, on the order of minutes to several days (Table 2). These results are consistent with previous studies that have focused on magmatic processes (e.g., Mackwell and Kohlstedt 1990; Demouchy and Mackwell 2006; Demouchy et al. 2006). At 1000°C, re-equilibration timescales range from tens of minutes to about a week for 1 mm models and an hour to several weeks for 3 mm models (Figure 4 and Table 2). In general, the cpx and olivine proton-polaron models are fastest (minutes to tens of minutes).

To determine the upper and lower bounds of uncertainty for re-equilibration timescales, 100 additional models were run for both 1 mm and 3 mm grain sizes (Figure 4). Re-equilibration timescales for upper and lower bounds on experimental uncertainties vary between minerals, but typically have the greatest uncertainty at 600°C and 1200°C. Model results do not perfectly mirror the error envelopes calculated in Figures 1 and 2, primarily due to different uncertainties on D_H values for the [100], [010], and [001] axes (Table S1) influencing anisotropic volume diffusion within a single model.

Uncertainties (open symbols in Figure 4) are overall lowest at 800°C, with the cpx and olivine proton-polaron model re-equilibrating in a few hours, opx and the olivine "total" models over several days to a week, and the olivine proton-vacancy slowest at several months to a year (Figure 5). Uncertainties are larger on 700°C models, where distinctions between mineral re-equilibration timescales are less clear. The olivine proton-vacancy models have the highest uncertainty, ranging from days to decades (Figure 5). Opx has the largest uncertainty at 1000°C, spanning nearly the combined range of the other two minerals.

Modeled cpx and olivine proton polaron timescales at 600°C range from hours to months and are relatively fast compared to opx re-equilibration, which occurs over months to hundreds of years. The other models overlap significantly within uncertainty at 600°C (Figure 5). The uncertainty associated with the proton-vacancy mechanism results in timescales ranging from about a day to several thousand years, corresponding to the entire range of timescales in the other 600°C models (Figure 5).

A final 12 models (3 cpx and 3 opx each for 1 and 3 mm models) were run to estimate the possible re-equilibration timescales of pyroxenes dominated by the proton-vacancy diffusion mechanism. For temperatures of 600-1000°C, the pyroxene model results from Figure 5 are compared to models that utilized slower diffusion coefficients that might better represent pyroxene vacancy diffusion mechanisms (Figure 6). Clinopyroxene proton-vacancy models using the D_H for synthetic diopside (0.7 wt% FeO; Sundvall et al. 2009; purple diamonds) range from a few months to a year at 1000°C and up to >100 kyr at 600°C (see also Table S3). These timescales are much slower than the clinopyroxene proton-polaron models using diffusion coefficients from Ferriss et al. (2016; purple squares), which are minutes to hours at 1000°C and several weeks at 600°C (Figure 6). The orthopyroxene proton-polaron (Stalder and Skogby, 2003; red squares) and vacancy (Stalder and Behrens, 2006; red diamonds) models are more congruent, yielding similar timescales that range from several hours at 1000°C to about a year at 600°C (Table S3).

We constrained the variability introduced by non-ideal sections using the 1 mm, 1000°C orthopyroxene model after 13.5 minutes of simulated diffusion (equal to 50% re-equilibration with the boundary condition). A subset of representative slices (Supplementary Figure S2) demonstrates that progressively off-center sections yield core water contents that are increasingly more re-equilibrated compared to the central core value. The average % re-equilibration from the 200 random slices is 65%, compared to the 50% measured at the core voxel of the ideal section through the crystal model. Only 17% of the 200 slices have water contents equal to the ideal core value (50% re-equilibration), and the remaining 83% of slices have % re-equilibration values greater than the central voxel value.

Discussion

Proton-polaron vs. proton-vacancy diffusion mechanisms in pyroxenes

In olivine, two diffusion mechanisms (proton-polaron and proton-vacancy) have been shown to control H^+ diffusion (e.g., Mackwell and Kohlstedt 1990; Kohlstedt and Mackwell 1998). It is likely that both mechanisms also operate in pyroxenes (e.g., Ingrin and Blanchard 2006 and references therein). The limiting factor in modeling pyroxene proton-vacancy diffusion is that very few studies have distinguished both mechanisms in cpx or opx, especially for experiments with Fe-bearing starting materials (e.g., Stalder and Skogby 2003, Sundvall et al. 2009; Yang et al. 2019). In this section we assess the potential differences in likely re-equilibration timescales when using proton-polaron vs. proton-vacancy diffusion data.

Most of our pyroxene models utilize proton-polaron diffusivities derived from dehydration experiments because they are the best constrained coefficients for Fe-bearing minerals. The timescales presented in Figure 5 are likely associated with the proton-polaron mechanism. Hence, our results are best applied to H^+ mobility in xenolith NAMs occurring over short timescales and may underestimate the re-equilibration of abyssal and orogenic pyroxenes over longer timescales. For these applications, the slower proton-vacancy mechanism may dominate diffusion behavior, but presently the vacancy mechanisms for cpx and opx are best constrained by experiments based on synthetic Fe-free or low-Fe starting material (e.g., Stalder and Skogby, 2003; Stalder and Behrens, 2006; Sundvall et al. 2009).

Despite the relative lack of proton-vacancy diffusion data for natural pyroxenes, we can estimate the vacancy diffusion rates and re-equilibration timescales by applying a slowness factor to our proton-polaron model results. The diffusion of metal vacancies (D_{VMe}) is ~3x slower than the effective diffusivity of H in olivine (e.g., proton-polaron mechanism; Kohlstedt and Mackwell, 1998), which limits H diffusion via the proton-vacancy mechanism. Slower H diffusion limited by D_{VMe} in pyroxenes is also likely (Ingrin and Blanchard, 2006), but largely unconstrained for natural cpx and opx compositions. One approach for estimating proton-vacancy controlled re-equilibration timescales is to multiply our modeled cpx and opx proton-polaron timescales (Figure 5, Table 2) by a factor of three, following the relationship established for olivine (Kohlstedt and Maxwell, 1998). This would approximate the re-equilibration timescales that might be likely for longer duration diffusion events, including metasomatism and hydrothermal alteration.

Another perspective on the slower vacancy-controlled diffusion mechanism in pyroxenes is provided by our models that utilize D_H from the hydration experiments of Sundvall et al. (2009; cpx) and Stalder and Behrens (2006; opx). These results provide examples of slower diffusion coefficients derived from synthetic Fe-free or low-Fe pyroxenes (Figure 6). While the opx proton-polaron (red squares) and proton-vacancy (red diamonds) models seem to reasonably reflect 3x slower re-equilibration timescales for the vacancy mechanism, the clinopyroxene results are not consistent with this approximation. Re-equilibration via the low-Fe (0.7 wt% FeO) cpx diffusion coefficient (purple diamonds, Figure 6; Sundvall et al. 2009) is several orders of magnitude slower than the proton-polaron mechanism (purple squares). This could be related to the significant compositional differences between the experimental starting materials. Sundvall et al. (2009) used synthetic diopside that contained 0.7 wt% FeO, whereas Ferriss et al. (2016) used Jaipur diopside containing 2.5 wt% FeO. More experimental datasets constraining the proton-vacancy mechanism for Fe-bearing pyroxene compositions are needed to resolve these issues.

Effective %re-equilibration

The re-equilibration timescales presented here are conservative estimates of the maximum time required to completely overprint NAM water contents. In the Supplementary Material, we evaluate the analytical errors associated with measuring NAM water contents in peridotites. We then calculate effective %re-equilibration timescales using Eq. 1, with the $H_{equilibrium}$ value for the boundary condition reflecting 1% and 10% analytical error.

Effective re-equilibration timescales (Supplementary Tables S4 and S5) are shorter than the 100% re-equilibration timescales because the rate at which the composition changes slows dramatically after about 60% re-equilibration. This effect is shown for 1 mm opx models at 1000ºC in Figure 7. The change in composition in the models is a function of both the diffusion coefficient (D_H) and the magnitude of the concentration gradient or chemical potential gradient. Based on Fick's 1st law, diffusive fluxes at a given point along a zoned profile are smaller when concentration gradients are shallower (Crank 1975). As diffusion causes the models to re-equilibrate, the compositional contrast between the crystal core and rim is reduced, leading to a decrease in the magnitude of the diffusive flux as the concentration shallows. Hence, a much smaller change in concentration occurs per unit of time and re-equilibration of smaller compositional contrasts is slower compared to larger contrasts (e.g., Zhang 2010).

With increasing time elapsed, the progressively shallower gradient yields much lower fluxes, and thus slower rates of re-equilibration, despite constant D_H. After ~90% re-equilibration the rate of change slows substantially (Figure 7) and the additional time required to reach 100% re-equilibration more than doubles the total modeled diffusion time. Thus, even 1-2% analytical uncertainty significantly reduces the timescales of our models. This effect is shown in Supplementary Figure S3 and listed in Table 1 for each mineral.

Effective %re-equilibration values were used to extract effective timescales from the models using the low-H and high-H silicate melt boundary conditions (Supplementary Material). Overall, an analytical uncertainty of 1% results in effective re-equilibration timescales that are typically ~30% shorter than the 100% re-equilibration timescales (Supplementary Table S5). Analytical uncertainty of 10% results in effective re-equilibration timescales that are ~60-70% shorter than the modeled 100% re-equilibration results (Table S5).

The effects of good vs. poor analytical precision are shown in Figure 8 by extracting cpx profiles at regular time intervals within the high-H model at 3 mm grain size and 1200°C. As diffusive re-equilibration affects the cpx core composition, the gradient between core and rim water contents becomes shallower. With increasing time elapsed, the magnitude of zoning in a 1D traverse across a natural pyroxene grain diminishes and becomes more difficult to resolve analytically. This analytical limit means that the last three clinopyroxene profiles in Figure 8 would not be resolvable when analytical precision is poor, for our boundary conditions. At 86% of the model re-equilibration (e.g., effective %re-equilibration at 10% analytical error), the effective timescale is ~3 minutes compared to the 100% timescale of 6 minutes (Table S5). This indicates that in natural samples, analyses of clinopyroxene would appear to be non-zoned after ~3 minutes of diffusion at 1200ºC, at which point they would be re-equilibrated past their H^+ kinetic window.

These effective re-equilibration timescales reinforce our interpretation that the modeled timescales presented here are conservative maximum estimates for constraining the kinetic window of H in NAMs. Effective re-equilibration timescales calculated from 1-2% error on the SIMS count statistics are overall ~30% shorter than the 100% re-equilibration timescales. If poorer analytical conditions result in 10% uncertainty, the modeled timescales are typically 60-70% shorter than the 100% re-equilibration timescales. Even with high precision analyses (i.e., 1-2% error), resolving 1D zoning will be challenging in NAMs that have neared complete re-equilibration with surrounding silicate melts or aqueous fluids.

Overprinted NAM water contents

The compositions of peridotites often indicate a complex history that includes partial melting and melt-rock interaction, with subsequent hydrothermal alteration (aqueous fluid-rock interaction). Given the short timescales over which NAMs can re-equilibrate at 600-1200°C (Figure 5), melt-and fluid-rock interactions can modify water contents of residual peridotites after partial melting has ceased. Here we explore the potential of hydrogen diffusion for constraining the timescales of melt-rock and fluid-rock interaction processes.

Xenoliths. The only mantle peridotites likely to preserve grain-scale zonation are xenoliths due to fast magma ascent rates (e.g., >0.06-0.20 m/s have been estimated for xenoliths based on FeMg zoning in olivine [Klugel et al. 1997] and fluid dynamic models [Spera 1984]). However, diffusion timescales associated with xenoliths are unlikely to reflect mantle processes. Instead, hydrogen gradients in xenoliths typically reflect volatile loss due to decompression during ascent (e.g., Demouchy et al. 2006; Peslier et al. 2008; Tian et al. 2017; Denis et al. 2018).

Our model results at 1200°C provide additional insights on how quickly mantle water contents are overprinted after they are entrained in a carrier magma, as well as the timescales over which core water contents are subsequently lost during degassing. As shown in Figure 5, complete re-equilibration of 1-3 mm grains at 1200°C could occur in minutes to 10's of minutes (cpx proton-polaron, olivine proton-polaron) or a few hours up to a few days (opx proton-polaron, olivine total, olivine vacancy) at 1200°C. Effective re-equilibration timescales can be twice as fast, indicating that xenolith NAMs are highly susceptible to diffusive overprinting while entrained in the carrier magma. Off-center sectioning (Supplementary Figure S2) would increase the likelihood that measured H contents in xenolith NAMs are quickly overprinted. Our models were run simulating a silicate melt completely surrounding a grain (Figure 3) and thus are most relevant for mantle xenocrysts or NAMs on the exterior of an ascending xenoliths. Grains in the interior of a xenolith would be more resilient to overprinting than indicated by these results and should ideally be treated using a multi-mineral aggregate 3D model that can also treat grain boundary diffusion (e.g., Fisher 1951; Demouchy 2010).

Xenoliths entrained in parental melts typically spend much longer than hours to days in the host magma prior to the degassing histories recorded by the hydrogen profiles. Diffusion of Ni in Fo_{90} olivine from Irazu Volcano (Costa Rica) suggests that “fast” ascent of arc mantle melts from the Moho (~35 km depth) occurs over months to years (Ruprecht and Plank 2013). Zoning of FeMg in xenolith olivine from La Palama (Canary Islands) indicates entrainment of 8-110 years in the carrier magma prior to ascent to the surface (Klugel et al. 1997). Diffusion modeling of Fe-Mg, Ni, Mn, and Ca zoning in xenolith olivine from Upper Placeta San Pedro lavas (Chilean Andes) also indicate residence timescales of several months to ~25 years (Costa et al. 2005). Given these long transport timescales from mantle depths to eruption at the surface, it is unlikely for even interior NAMs to preserve mantle water signatures. The xenoliths most likely to retain mantle water contents are those carried by kimberlites. Interdiffusion of Fe-Mg in megacryst ilmenite from kimberlite xenoliths indicates residence timescales on the order of a few hours prior to eruption (Prissel et al. 2020). Experimental studies of dissolution reactions in garnet lherzolite also suggest that kimberlite xenoliths may spend <1 hour in 1200ºC magma prior to eruption (Canil and Ferdortchouck 1999).

Massif and abyssal peridotites. The short timescales from our numerical diffusion models highlight the susceptibility of NAM water contents to being overprinted by late-stage processes. The water contents of NAMs in peridotites exposed on the ocean floor and as massifs on land are often interpreted to record mantle water left behind after partial melting (e.g., Gose et al. 2009; Peslier 2010; Schmädicke et al. 2011; Warren and Hauri 2014; Kumamoto et al. 2019).

However, these samples undergo very long durations of cooling prior to exposure on the Earth's surface. For example, Warren et al. (2009) estimated that peridotites from the ultraslow spreading Southwest Indian Ridge can take up to ~13 Myr to cool from 1200°C to 0°C. During this long uplift history, NAMs are susceptible to melt-rock or aqueous fluid-rock interactions that can diffusively modify their water contents (e.g., Kumamoto et al. 2019). The fast re-equilibration times in our models compared to these long cooling histories suggest that peridotite NAMs are unlikely to preserve core-rim zoning from diffusive re-equilibration (e.g., inside the kinetic window of H^+). Instead, water contents may be overprinted by diffusive re-equilibration that progressed past the kinetic window of hydrogen. Below, we explore the potential of silicate melt-rock and aqueous fluid-rock interaction to modify the hydrogen content of abyssal and massif peridotites.

Melt-rock interactions

The timescales of melt-rock interaction in the mantle are poorly constrained. Ophiolitic, orogenic, and abyssal peridotites can exhibit melt-rock interaction in the form of channels and veins at centimeter to meter length scales (e.g., Kelemen and Dick 1995; Python and Ceuleneer 2003). In other cases, samples lack obvious veins, but their textures and compositions suggest diffusive melt flow through the rock (e.g., Seyler et al. 2001; Python and Ceuleneer 2003; Warren and Shimizu 2010; Kumamoto et al. 2019; Ashley et al. 2020). Temperatures associated with infiltrating melts in the upper mantle range from 600-1100°C (Python and Ceuleneer 2003). Our model results show that, over this temperature range, NAM water contents can diffusively re-equilibrate in individual crystals within minutes to several years as a result of melt-rock interactions (Figure 5). Effective re-equilibration timescales could be as fast as several months. If melt channels or films are ephemeral, even partial re-equilibration is likely to occur and subsequent diffusion into the crystal core will ultimately overprint original mantle water contents.

These short model timescales can resolve discrepancies between measured water contents and mineral trace elements in some peridotites at mid-ocean ridges. Peridotite rare earth element (REE) patterns at the Southwest Indian Ridge are reproduced well by partial melting models, but NAM H_2O contents are too high to reflect residues of melting (Warren and Hauri 2014). Rapid diffusion of hydrogen, even at the intermediate temperatures used in our models, would decouple NAM water contents from the other trace elements, which are much slower diffusing species. Over the 600-1200°C temperature range investigated here, diffusivities for rare earth elements (Dy, Yb, Nd, Ce, Lu) in cpx are 10^{-20} to 10^{-32} (Van Orman et al. 2001), which are 7-19 orders of magnitude slower than hydrogen ($D_H^{cpx} = 10^{-9}$ to 10^{-13}; Woods et al. 2000). Nominally anhydrous minerals in residual peridotites that have dehydrated during melting would re-equilibrate H^+ with basaltic melts (e.g., mid-ocean ridge basalt contains 0.1-1.5 wt% H_2O; Dixon et al. 2002). Our models suggest that H re-equilibration of these Southwest Indian Ridge samples could have occurred in as little as a few minutes to a few days (Figure 5). Re-enrichment of the REEs would take several orders of magnitude longer durations due to their much slower diffusion coefficients. At the same time and temperature conditions, no re-enrichment of the REEs would be expected while complete H re-equilibration could easily occur. Thus, interaction of a melt with the mantle could quickly hydrate residual NAMs at temperatures where other trace elements are immobile.

Our numerical models also help to explain variations in orthopyroxene water contents that are decoupled from other trace element variations in the Josephine Peridotite. Transects by

Kumamoto et al. (2019) across shear zones in the Josephine Peridotite identified variations in LREE contents over spatial scales of several meters, inferred to be a result of melt-rock interaction. The water content in orthopyroxene is also variable across the transects, but decoupled from other trace element variations. This suggests that H fully re-equilibrated with a melt or hydrothermal fluid up to the maximum storage capacity of orthopyroxene (based on trivalent element chemistry). Orthopyroxene water contents up to 350 ppm were measured near the center of one of the shear zones, where an interstitial melt is inferred to have driven diffusive re-equilibration at 900-1000ºC (Kumamoto et al. 2019). Based on our numerical models, these orthopyroxene water contents could fully re-equilibrate with a silicate melt or high-temperature hydrothermal fluid within 1-8 hours (Figure 5). If error envelopes for the diffusion coefficients are considered, this time expands to minutes to a few weeks, still within a relatively short time-scale.

The net result of melt-rock interactions between a depleted residual peridotite and a partial melt will be an increase in overall NAM water content, even if NAMs only partially re-equilibrate during melt flow. Because H^+ diffusion in each NAM has a different rate at a given temperature, the cessation of melt flow at a given time might be reflected by different degrees of re-equilibration between cpx, olivine, and opx. This is particularly relevant for our lower model temperatures, where the 100% re-equilibration timescales require melt flow for a few weeks to over a year for the different mineral phases (Figure 5). Dis-equilibrium water contents between NAM phases could thus reflect differences in activation energy between Arrhenius relationships at a given temperature (Xu et al. 2019) and H^+ diffusion may be useful for deciphering the timescales of this process.

Aqueous fluid-rock Interactions

Peridotite hydrothermal alteration due to aqueous fluid-rock interactions have previously been interpreted to have little diffusive effect on NAM water contents (e.g., Gose et al. 2011; Warren and Hauri 2014). Simplified 1D calculations at 600ºC suggest that 10’s to 100’s of years are required for diffusion distances to reach beyond 1 mm (Gose et al. 2011). In light of our improved model constraints on H^+ re-equilibration timescales, we revisit the possibility that hydrothermal alteration processes may affect anhydrous mineral water contents.

Serpentine can be stable up to ~700°C (Ulmer and Trommsdorff 1995), though stability is limited to ~500°C in multiphase assemblages (Guillot et al. 2015). This range of temperature overlaps with our models and is close to the lowest temperatures at which H^+ diffusion coefficients have been measured (Figures 1 and 2). In addition, fluid driven peridotite alteration can extend to even higher temperatures, where assemblages such as tremolite ± talc± serpentine ± chlorite form at the expense of pyroxene (Bach et al. 2004; Früh-Green et al. 2004; Bach and Klein 2009; Fumagalli et al. 2009; Klein et al. 2015; Prigent et al. 2020). For example, tremolite, usually found in rims around pyroxene grains, is stable up to ~850 °C at 0.3–1.0 GPa (e.g., Chernosky et al. 1998). Although this reaction environment has low silica activity, which would favor H incorporation in the olivine [Si] defect (Kempf and Hermann 2018), the relatively high temperatures (>600ºC) promote inter-site reactions that remove H^+ from the [Si] site and subsequent diffusion is likely dominated by a much faster pathway (e.g., proton-polaron or proton-vacancy; Jollands et al. 2019). Even if silica activity influences diffusion in olivine this effect has not been identified in pyroxenes. Most NAM water measurements in abyssal peridotites are made on pyroxenes as olivine is typically extensively altered and also more challenging to measure due to its lower water contents.

During high-temperature alteration, the H^+ content of olivine is predicted by our models to re-equilibrate in hours to months at 800°C, with effective timescales ranging from hours to days (Tables 2 and 3). At 600°C, complete re-equilibration would occur over days to years, with the caveat that high uncertainties on the olivine proton-vacancy timescales yield years to hundreds of years (Figure 5). Pyroxenes, although simultaneously reacting with the hydrothermal fluids to form amphibole, would also re-equilibrate via the proton-polaron mechanism over timescales of hours to days at 800°C and weeks to months at 600°C (Figure 5). If the proton-vacancy mechanism dominates at these intermediate temperatures, timescales may be 3x longer than the proton-polaron models suggest (Ingrin and Blanchard, 2006). These durations at 600ºC are much shorter than estimates made from 1D calculations, which require 21 years for diffusion to even reach the core of a 3 mm orthopyroxene crystal (using $x=(D*t)^{1/2}$, following Gose et al. 2011 and using D_H^{opx} for the proton-polaron mechanism from Stalder and Skogby 2003). This illustrates the importance of considering the flux of elements in three dimensions rather than using simplified estimates of 1D diffusion distance to assess re-equilibration potential.

Peridotites that have been the focus of NAM studies preserve relics of primary minerals, indicating that those samples have not undergone intense hydrothermal alteration. In abyssal peridotites from the Southwest Indian Ridge, Warren and Hauri (2014) measured 650-800 ppm H_2O in cpx and 300-400 ppm H_2O in opx in samples where pyroxene had been partially altered to tremolite, which is stable up to 850°C (Chernosky et al. 1998). These water contents are higher by ~400 ppm for cpx and ~150 ppm for opx than water contents of pyroxenes in less altered samples collected from the same area. These observations suggest that aqueous fluid-rock interactions can increase pyroxene water contents during the reaction to form tremolite. Our models predict that these relatively H_2O-rich pyroxenes could have been hydrated by an aqueous fluid flowing over timescales of only hours to days.

Our model, though it relies on the assumption that fluid flow is continuous (e.g., a static boundary condition), shows that H^+ diffusion is significant during high-T hydrothermal alteration. Fluid flow in ultramafic rocks is probably variable in time and space and thus fluid-driven diffusion is unlikely to be a constant process (e.g., Roumejon and Cannat 2014; Roumejon et al. 2015). However, the modeled timescales of days to weeks are short compared to the lifetimes of hydrothermal systems, which have been estimated at 10^1-10^6 yr (Finkel et al. 1980; Kadko 1996; Cathles et al. 1997; Früh-Green et al. 2003; Gose et al. 2011). Even though the timescales of hydrogen re-equilibration in NAMs are short relative to the lifespans of hydrothermal systems, the duration of fluid flow driving diffusion cannot be so long that the minerals fully react out to serpentine, tremolite, and other hydrous phases. Comparing the modeled re-equilibration timescales to the rates of high-T alteration or serpentinization is difficult because most of the experimental work has been conducted at temperatures of 300ºC or less (Martin and Fyfe 1970; Wegner and Ernst 1983; Malvoisin et al. 2012; Godard et al. 2013; Malvoisin and Brunet 2014; Klein et al. 2015). However, our models do suggest that even if NAM water contents are not completely overprinted during fluid flow, diffusion could generate H^+ zoning profiles within the residual primary minerals, especially at the lower-T end of the range investigated by our models.

Implications

The 3D diffusion modeling approach that we have presented provides constraints on the potential for NAM water contents to re-equilibrate with silicate melts and/or aqueous fluids over the temperature range 600-1200°C. Distinguishing between melt- and fluid-driven diffusion is a major challenge for studies of hydrogen in massif and abyssal peridotites because of the potential for both processes to have occurred. Our models show that NAM hydrogen contents can re-equilibrate within minutes to weeks at 1000-1200°C and hours to several years at 600-800°C (Figure 5), though pyroxene timescales could be longer if the proton-vacancy mechanism dominates pyroxene diffusion (Figure 6). Effective % re-equilibration timescales could decrease those ranges by half, indicating that silicate melt-rock and aqueous fluid-rock interactions can significantly modify NAM water contents over geological timescales.

These models also show that decoupling of NAM water contents from their REE abundances (e.g., Warren and Hauri 2014; Peslier et al. 2017; Ashley et al. 2020) can be caused by both melt-rock and/or fluid-rock interactions at temperatures > 600°C. As such, characterizing hydrothermal alteration phase assemblages and identifying evidence for melt addition are important for interpreting residual NAM water contents. Alone, the hydrogen content of NAMs is not indicative of either melt or aqueous fluid driven re-equilibration. Unraveling the origin of the water contents measured in peridotite NAMs requires additional constraints on the history of the sample, including petrographic analysis and measurement of other trace elements.

If NAM water contents are partially re-equilibrated during hydrothermal alteration, H^+ chronometry can also potentially be used to extract the timescale of the fluid flow process. This will require careful analytical work and that the temperature of alteration can be constrained, so that diffusion profiles can be modeled. At present, several unknown parameters limit this application. Constraints on the solubility of water in NAMs at low temperature are needed to determine the maximum amount of H^+ that can diffuse into silicate minerals surrounded by an extremely high boundary condition and chemical potential (e.g., an excess of liquid water in the system). As fluid percolation also drives chemical exchange during fluid-rock interactions, future applications in natural samples will need to allow for moving boundary conditions (e.g., crystal growth or dissolution) within multi-mineral aggregates.

Diffusion during low-T serpentinization?

The new insights from our modeling open up the possibility that NAMs may re-equilibrate over a much larger temperature range than previously appreciated. Serpentinization occurs over temperatures from <50°C to >500°C (Guillot et al. 2015). The presence of fluids during this process may cause considerable hydration of NAMs depending on the rate of diffusion compared to the rate of the serpentinization reaction. At temperatures below ~400°C, and possibly down to < 50°C, pyroxenes are stable during hydrothermal alteration, while olivine alters to form serpentine + brucite (Alt et al. 2007; Bach et al. 2004; Bach and Klein 2009; Klein et al. 2015). Contrary to previous interpretations (e.g., Gose et al. 2011; Warren and Hauri 2014), our models suggest that aqueous fluid-rock interactions at temperatures of 500°C or less may modify at least clinopyroxene water contents, which might be partially overprinted by diffusion in weeks to months at 600°C (Figure 5). Although hydration of pyroxene during low-T serpentinization of olivine may be possible, further experimental constraints for D_H at temperatures < 700°C are needed. In addition, inter-site reactions may also affect the diffusion coefficients at such low temperatures (e.g., Jollands et al. 2019). Current high temperature (e.g., > 700ºC) diffusion rates for NAMs are characteristic of diffusion in transition metal-bearing materials at intermediate temperatures (TaMED mechanism; Chakraborty 2008). Re-equilibration driven by the lower temperatures of serpentinization may instead be dominated by pure extrinsic diffusion, which likely has a different activation energy and thus a different slope on the Arrhenius diagram.

Acknowledgements

We thank Thomas Shea for initial model guidance, Henry Towbin for fruitful discussions on xenolith water contents, Adam Wallace for access to the University of Delaware High Performance Community Cluster, Anita Schwartz for model optimization on the cluster, and Sylvie Demouchy for comments on a previous version of this paper. We thank Anne Peslier for excellent editorial handling and three anonymous reviewers for thorough comments that substantially improved this manuscript. This study was supported by U.S. National Science Foundation grants EAR-1255620 and EAR-1625032 to J.M. Warren.

References Cited

Achenbach, K.L., Cheadle, M.J., Faul, U.H., Kelemen, P.B., and Swapp, S.M. (2011) Lattice-preferred orientation and microstructure of peridotites from ODP Hole 1274A (15°39∙N), Mid-Atlantic Ridge: Testing models of mantle upwelling and tectonic exhumation. Earth and Planetary Science Letters, 301, 199–212. https://doi.org/10.1016/j.epsl.2010.10.041

Alt, J.C., Shanks III, W.C., Bach, W., Paulick, H., Garrido, C.J., and Beaudoin, G. (2007) Hydrothermal alteration and microbial sulfate reduction in peridotite and gabbro exposed by detachment faulting at the Mid-Atlantic Ridge, 15º20’N (ODP Leg 209): A sulfur and oxygen isotope study. Geochemistry Geophysics Geosystems, 8, 1-22. https://doi.org/10.1029/2007GC001617

Ashley, A.W., Bizimis, M., Peslier, A.H., Jackson, M., and Konter, J. (2020) Metasomatism and hydration of the oceanic lithosphere: A case study of peridotite xenoliths from Samoa. Journal of Petrology, in press. https://doi.org/10.1093/petrology/egaa028

Bach, W., and Klein, F. (2009) The petrology of seafloor rodingites: Insights from geochemical reaction path modeling. Lithos, 112, 103-117. https://doi.org/10.1016/j.lithos.2008.10.022

Bach, W., Garrido, C.J., Paulick, H., Harvey, J., and Rosner, M. (2004) Seawater-peridotite interactions: First insights from ODP Let 209, MAR 15ºN. Geochemistry Geophysics Geosystems, 5, 1-22. https://doi.org/10.1029/2004GC000744

Barth, A., Newcombe, M., Plank, T., Gonnermann, H., Hajimirza, S., Soto, G.J., Saballos, A., and Hauri, E. (2019) Magma decompression rate correlates with explosivity at basaltic volcanoes – Constraints from water diffusion in olivine. Journal of Volcanology and Geothermal Research, 387, 10664. https:/doi.org/10.1016/j.jvolgeores.2019.106664

Bell, D.R., Ihinger, P.D., and Rossman, G.R. (1995) Quantitative analysis of trace OH in garnet and pyroxenes. American Mineralogist, 80, 465-474.

Boullier, A.-M., and Nicolas, A. (1975) Classification of textures and fabrics of peridotite xenoliths from South African kimberlites. Physics and Chemistry of the Earth, 9, 467–468. https://doi.org/10.1016/B978-0-08-018017-5.50037-7

Cathles, L.M., Erendi, H.J., and Barrie, T. (1997) How long can a hydrothermal system be sustained by a single intrusive event? Economic Geology, 92, 766-771. https://doi.org/10.2113/gsecongeo.92.7-8.766

Canil, D., and Fedortchouk, Y. (1999) Garnet dissolution and the emplacement of kimberlites. Earth and Planetary Science Letters, 167, 227-237.

Chakraborty, S. (2008) Diffusion in solid silicates: A tool to track timescales of processes comes of age. Annual Reviews in Earth and Planetary Science, 36, 153-190.

Chernosky, J.V., Berman, R.G., and Jenkins, D.M. (1998) The stability of tremolite: New experimental data and thermodynamic assessment. American Mineralogist, 83, 726-739. https://doi.org/10.2138/am-1998-7-805

Costa, F., and Chakraborty, S. (2008) The effect of water on Si and O diffusion rates in olivine and implications for transport properties and processes in the upper mantle. Physics of the Earth and Planetary Interiors, 166, 11-29. doi: 10.1016/j.pepi.2007.10.006

Costa, F., and Dungan, M. (2005) Short timescales of magmatic assimilation from diffusion modeling of multiple elements in olivine. Geology, 33, 837-840. https://doi.org/10.1130/G21675.1

Costa, F., Chakraborty, S., and Dohmen, R. (2003) Diffusion coupling between trace and major elements and a model for calculation of magma residence times using plagioclase.

Geochimica et Cosmochimica Acta, 67(12), 2189-2200. https://doi/org/10.1016/S0016-7037(02)01345-5

Crank, J. (1975) The Mathematics of Diffusion, 2nd ed.: Oxford Science Publications, Oxford, 415 p.

Demouchy, S. (2010) Hydrogen diffusion in spinel grain boundaries and consequences for chemical homogenization in hydrous peridotite. Contributions to Mineralogy and Petrology, 160, 887-898. doi: 10.1007/s00410-010-0512-4

Demouchy, S., Thoraval, C., Bolfan-Casanova, N., and Manthilake, G. (2016) Diffusivity of hydrogen in iron-bearing olivine at 3 GPa: Physics of the Earth and Planetary Interiors. 260, 1-13. doi: 10.1016/j.pepi.2016.08.005

Demouchy, S., and Mackwell, S. (2006) Mechanisms of hydrogen incorporation and diffusion in iron-bearing olivine. Physics and Chemistry of Minerals, 33, 347-355. https://doi.org/10.1007/s00269-006-0081-2

Demouchy, S., Jacobsen, S.D., Gaillard, F., and Stern, C.R. (2006) Rapid magma ascent recorded by water diffusion profiles in olivine from Earth's mantle. Geology, 34, 429-432.

Denis, C.M.M., Demouchy, S., and Alard, O. (2018) Heterogeneous hydrogen distribution of orthopyroxene from veined mantle peridotite (San Carlos, Arizona): Impact of melt-rock interactions. Lithos, 302-303, 298-311. https://doi.org/10.1016/j.lithos.2018.01.007

Denis, C.M.M., Alard, O., and Demouchy, S. (2015) Water content and hydrogen behavior during metasomatism in the uppermost mantle beneath Ray Pic volcano (Massif Central, France). Lithos, 236-237, 256-274. https://doi.org/10.1016/j.lithos.2015.08.013

Dixon, J.E., Leist, L., Langmuir, C., and Schilling, J-G. (2002) Recycled dehydrated lithosphere observed in plume-influenced mid-ocean-ridge basalt. Nature, 420, 385-389. https://doi.org/10.1038/nature01215

Dohmen, R., and Chakraborty, S. (2007a) Fe-Mg diffusion in olivine II: point defect chemistry, change of diffusion mechanisms and a model for calculation of diffusion coefficients in natural olivine. Physics and Chemistry of Minerals, 34, 409-430. https://doi.org/10.1007/s00269-007-0158-6

Dohmen, R., and Chakraborty, S. (2007b) Erratum to Fe-Mg diffusion in olivine II: point defect chemistry, change of diffusion mechanisms and a model for calculation of diffusion coefficients in natural olivine. Physics of Chemistry and Minerals, 34, 597-598. https://doi.org/10.1007/s00269-007-0185-3

Faul, U.H., Cline, C.J., David, E.C., Berry, A.J., and Jackson, I. (2016) Titanium-hydroxyl defect-controlled rheology of the Earth’s upper mantle. Earth and Planetary Science Letters, 452, 227-237. https://doi.org/10.1016.j.epsl.2016.07.016

Ferriss, E., Plank, T., Newcombe, M., Walker, D., and Hauri, E. (2018) Rates of dehydration of olivines from San Carlos and Kilauea Iki. Geochimica et Cosmochimica Acta, 242, 165-190. https://doi.org/10.1016/j.GCA.2018.08.050

Ferriss, E., Plank, T., and Walker, D. (2016) Site-specific hydrogen diffusion rates during clinopyroxene dehydration. Contributions to Mineralogy and Petrology, 171, 55. https://doi.org/10.1007/s00410-016-1262-8

Finkel, R.C., Macdougall, J.D., and Chung, Y.C. (1980) Sulfide precipitates at 21°N on the East Pacific Rise: ^{226}Ra, ^{210}Pb, and ^{210}Po. Geophysical Research Letters, 7, 685-688. https://doi.org/10.1029/GL007i009p00685

Fisher, J.C. (1951) Calculation of diffusion penetration curves for surface and grain boundary diffusion. Journal of Applied Physics, 22, 74-77. https://doi.org/10.1063/1.1699825

Früh-Green, G.L., Connolly, J.A.D., Plas, A., Kelley, D.S., and Grobéty B (2004) Serpentinization of oceanic peridotites: Implications for geochemical cycles and biological activity. American Geophysical Union Monograph, 144, 119-136.

Fumagalli, P., Zanchetta, S., and Poli, S. (2009) Alkali in phlogopite and amphibole and their effects on phase relations in metasomatized peridotites: a high-pressure study. Contributions to Mineralogy and Petrology, 158, 723-737. https://doi.org/10.1007/s00410-009-0407-4

Godard, M., Luquot, L., Andreani, M., and Gouze, P. (2013) Incipient hydration of mantle lithosphere at ridges: A reactive-percolation experiment. Earth and Planetary Science Letters, 371-372, 92-102. doi: 10.1016/epsl.2013.03.052

Gose, J., Schmädicke, E., and Stalder, R. (2011) Water in mantle orthopyroxene – no visible change in defect water during serpentinization. European Journal of Mineralogy, 23, 529-536. https://doi.org/10.1127/0935-1221/2011/0023-2122

Gose, J., Schmädicke, E., and Beran, A. (2009) Water in enstatite from Mid-Atlantic Ridge peridotite: Evidence for the water content of suboceanic mantle? Geology, 37, 543-546. https://doi.org/10.1130/G25558A.1

Guillot, S., Schwartz, S., Reynard, B., Agard, P., and Prigent, C. (2015) Tectonic significance of serpentinites. Tectonophysics, 646, 1-19. https://doi.org/10.1016/j.tecto.2015.01.020

Hiraga, T., Hirschmann, M.M., and Kohlstedt, D.L. (2007) Equilibrium interface segregation in the diopside-forsterite system II: Applications of interface enrichment to mantle geochemistry. Geochimica et Cosmochimica Acta, 71, 1281-1289. https://doi.org/10.1016/j.gca.2006.11.020

Hirschmann, M.M. (2006) Water, melting, and the deep Earth H_2O cycle. Annual Reviews in Earth and Planetary Science, 34, 629-653. https://doi.org/10.1146/annurev.earth.34.031405.125211

Hirth, G., and Kohlstedt, D.L. (1996) Water in the oceanic upper mantle: implications for rheology, melt extraction and the evolution of the lithosphere. Earth and Planetary Science Letters, 144, 93-108. https://doi.org/10.1016/0012-821X(96)00154-9

Ingrin, J., and Blanchard, M. (2006) Diffusion of hydrogen in minerals. Reviews in Mineralogy and Geochemistry, 62, 291-320.

Ingrin, J., and Skogby, H. (2000) Hydrogen in nominally anhydrous upper-mantle minerals: concentration levels and implications. European Journal of Mineralogy, 12, 543-570.

Jollands, M.C., and Müntener, O. (2019) Testing orthopyroxene diffusion chronometry on rocks from the Lanzo massif (Italian Alps). Journal of Geophysical Research: Solid Earth, 124. https://doi.org/10.1029/2018JB016963

Jollands, M.C., Kempf, E., Hermann, J., and Müntener, O. (2019) Coupled inter-site reaction and diffusion: Rapid dehydrogenation of silicon vacancies in natural olivine. Geochimica et Cosmochimica Acta, 262, 220-242. https://doi.org/10.1016/j.gca.2019.07.025

Jollands, M.C., Padrón-Navarta, J.A., Hermann, J., and O'Neill, H.S.C. (2016) Hydrogen diffusion in Ti-doped forsterite and the preservation of metastable point defects. American Mineralogist, 101, 1560-1570.

Kadko, D. (1996) Radioisotopic studies of submarine hydrothermal vents. Reviews in Geophysics, 4, 349-366. https://doi.org/10.1029/96RG01762

Kahl, M., Chakraborty, S., Costa, F., and Pompilio, M. (2011) Dynamic plumbing system beneath volcanoes revealed by kinetic modeling, and the connection to monitoring data: An example from Mt. Etna. Earth and Planetary Science Letters, 308, 11-22. https://doi.org/10.1016/j.epsl.2011.05.008

Kelemen, P.B., and Dick H.J.B. (1995) Focused melt flow and localized deformation in the upper mantle: Juxtaposition of replacive dunite and ductile shear zones in the Josephine peridotite, SW Oregon. Journal of Geophysical Research, 100, 423-438. https://doi.org/10.1029/94JB02063

Kempf, E.D., and Hermann, J. (2018) Hydrogen incorporation and retention in metamorphic olivine during subduction: Implications for the deep water cycle. Geology, 46, 571-574. https://doi.org/10.1130/G40120.1

Klein, F., Grozeva, N.G., Seewald, J.S., McCollom, T., Humphris, S.E., Moskowitz, B., Berquo, T.S., and Kahl, W-A. (2015) Experimental constraints on fluid-rock reactions during incipient serpentinization of harzburgite. American Mineralogist, 100, 991-1002. https://doi.org/10.2138/am-2015-5112

Klugel, A., Hansteen, T.H., Schminke, H-U (1997) Rates of magma ascent and depths of magma reservoirs beneath La Palma (Canary Islands). Terra Nova, 9, 117-121.

Kohlstedt, D.L., and Mackwell, S.J. (1998) Diffusion of hydrogen and intrinsic point defects in olivine: Zeitschrift für Physikalische Chemie, 207, 147-162.

Krimer, D., and Costa, F. (2017) Evaluation of the effects of 3D diffusion, crystal geometry, and initial conditions on retrieved time-scales from Fe-Mg zoning in natural oriented orthopyroxene crystals. Geochimica et Cosmochimica Acta, 196, 271-288. https://doi.org/10.1016/j.gca.2016.09.037

Kumamoto, K.M., Warren, J.M., and Hauri, E.H. (2019) Evolution of the Josephine Peridotite shear zones: Part I: Compositional variation and shear initiation. Geochemistry Geophysics Geosystems, 20. https://doi.org/.1029/2019GC008399

Lemaire, C., Kohn, S.C., and Brooker, R.A. (2004) The effect of silica activity on the incorporation mechanisms of water in synthetic forsterite: A polarized infrared spectroscopic study. Contributions to Mineralogy and Petrology, 147, 48-57. doi: 10.1007/s00410-003-0539-x

Le Voyer, M., Asimow, P.D., Mosenfelder, J.L., Guan, Y., Wallace, P.J., Schiano, P., Stolper, E.M., and Eiler, J.M. (2014) Zonation of H2O and F concentrations around melt inclusions in olivine. Journal of Petrology, 55, 685-707. https://doi.org/10.1093/petrology/egu003

Lloyd, A.S., Ferriss, E., Ruprecht, P., Hauri, E.H., Jicha, B.R., and Plank, T. (2016) An assessment of clinopyroxene as a recorder of magmatic water and magma ascent rate. Journal of Petrology, 57, 1865-1886. https://doi.org/10.1093/petrology/egw058

Lynn, K.J., Garcia, M.O., Shea, T., Costa, F., and Swanson, D.A. (2017a) Timescales of mixing and storage for Keanakākoʻi Tephra magmas (1500-1820 C.E.), Kīlauea Volcano, Hawaiʻi. Contributions to Mineralogy and Petrology, 172, 76. https://doi.org/10.1007/s00410-017-1395-4

Lynn, K.J., Shea, T., and Garcia, M.O. (2017b) Nickel variability in Hawaiian olivine: Evaluating the relative contributions from mantle and crustal processes. American Mineralogist, 102, 507-518. https://doi.org/10.2138/am-2017-5763.

Mackwell, S.J., and Kohlstedt, D.L. (1990) Diffusion of hydrogen in olivine: Implications for water in the mantle. Journal of Geophysical Research, 95, 5079-5088. https://doi.org/10.1029/JB095iB04p05079

Mackwell, S.J., Kohlstedt, D.L., and Paterson, M.S. (1985) The role of water in the deformation of olivine single crystals. Journal of Geophysical Research, 90, 11319-11333. https://doi.org/10.1029/JB090iB13p11319

Malvoisin, B., and Brunet, F. (2014) Water diffusion-transport in a synthetic dunite: Consequences for oceanic peridotite serpentinization. Earth and Planetary Science Letters, 403, 263-272. doi: 10.1016/j.epsl.2014.07.004

Malvoisin, B., Brunet, F., Carlut, J., Roumejon, S., and Cannat, M. (2012) Serpentinization of oceanic peridotites: 2. Kinetics and processes of San Carlos olivine hydrothermal alteration. Journal of Geophysical Research, 117, 10.1019/2011JB008842

Martin, B., and Fyfe, W.S. (1970) Some experimental and theoretical observations on the kinetics of hydration reactions with particular reference to serpentinization. Chemical Geology, 6, 185-202.

Mercier, J.-C.C., and Nicolas, A. (1975) Textures and fabrics of upper-mantle peridotites as illustrated by xenoliths from basalts. Journal of Petrology, 16, 454-487. https://doi.org/10.1093/petrology/16.1.454

Mosenfelder, J.L., Deligne, N.I., Asimow, P.D., and Rossman, G.R. (2006) Hydrogen incorporation in olivine from 2-12 GPa. American Mineralogist, 91, 285-294. https://doi.org/10.2138/am.2006.1943

Padrón-Navarta, J-A., and Hermann, J. (2017) A subsolidus olivine water solubility equation for the Earth's upper mantle. Journal of Geophysical Research: Solid Earth, 122, 9862-9880. https://doi.org/10.1002/2017JB-14510.

Padrón-Navarta, J-A., Hermann, J., and O'Neill, H.S.C. (2014) Site-specific hydrogen diffusion rates in forsterite. Earth and Planetary Science Letters, 392, 100-112. https://doi.org/10.1016/j.epsl.2014.01.055

Peslier, A.H. (2010) A review of water contents of nominally anhydrous natural minerals in the mantles of Earth, Mars, and the Moon. Journal of Volcanology and Geothermal Research, 197, 239-258. https://doi.org/10.1016/j.jvolgeores.2009.10.006

Peslier, A.H., Schönbächler, M., and Busemann, H. (2017) Water in the Earth's interior: Distribution and origin. Space Science Reviews, 212, 743-811. doi: 10.1007/s11214-017-0387-z

Peslier, A.H., Woodland, A.B., and Wolff, J.A. (2008) Fast kimberlite ascent rates estimates from hydrogen diffusion profiles in xenolithic mantle olivines from southern Africa. Geochimica et Cosmochimica Acta, 72, 2711-2722. https://doi.org/10.1016/j.gca.2008.03.019

Peslier, A.H., and Luhr, J.F. (2006) Hydrogen loss from olivines in mantle xenoliths from Simcoe (USA) and Mexico: Mafic alkalic magma ascent rates and water budget of the subcontinental lithosphere. Earth and Planetary Science Letters, 242, 302-319. https://doi.org/10.1016/j.epsl.2005.12.019

Prigent, C., Warren, J.M., Kohli, A.H., and Teyssier, C. (2020) Fracture-mediated deep seawater flow and mantle hydration on oceanic transform faults. Earth and Planetary Science Letters, 532, 115988. https://doi.org/10.1016/j.epsl.2019.115988

Prissel, K.B., Krawczynski, M.J., and Van Orman, J.A. (2020) Fe-Mg and Fe-Mn interdiffusion in ilmenite with implications for geospeedometry using oxides. Contributions to Mineralogy and Petrology, 175, 62. https://doi.org/10.1007/s00410-020-01695-z

Python, M., and Ceuleneer, G. (2003) Nature and distribution of dykes and related melt migration structures in the mantle section of the Oman ophiolite. Geochemistry Geophysics Geosystems, 4, 8612. https://doi.org/10.1029/2002GC000354

Roumejon, S., Cannat, M., Agrinier, P., Godard, M., and Andreani, M. (2015) Serpentinization and fluid pathways in tectonically exhumed peridotites from the Southwest Indian Ridge (62-65E). Journal of Petrology, 56, 703-734. https://doi.org/10.1093/petrology/egv014

Roumejon, S., and Cannat, M. (2014) Serpentinization of mantle-derived peridotites at mid-ocean ridges: Mesh texture development in the context of tectonic exhumation. Geochemistry Geophysics Geosystems, 15, 2354-2379. https://doi.org/10.1002/2013GC005148

Ruprecht, P., and Plank, T. (2013) Feeding andesitic eruptions with a high-speed connection from the mantle. Nature, 500, 68-72. https://doi.org/10.1038/nature12342

Ruth, D.C.S., Costa, F., Bouvet de Maisonneuve, C., Franco, L., Cortés, J.A., and Calder, E.S. (2018) Crystal and melt inclusion timescales reveal the evolution of magma migration before eruption. Nature Communications, 9, 2657. https://doi.org/10.1038/s41467-018-05086-8 |

Schmädicke, E., Gose, J., and Will, T.M. (2011) Heterogeneous mantle underneath the North Atlantic: Evidence from water in orthopyroxene, mineral composition and equilibrium conditions of spinel peridotite from different locations at the Mid-Atlantic Ridge. Lithos, 125, 308-320. https://doi.org/10.1016/j.lithos.2011.02.014

Seyler, M., Toplis, M.J., Lorand, J-P., Luguet, A., and Cannat, M. (2001) Clinopyroxene microtextures reveal incompletely extracted melts in abyssal peridotites. Geology, 29, 155-158. https://doi.org/10.1130/0091-7613(2001)029<0155:CMRIEM>2.0.CO;2

Shea, T., Lynn, K.J., and Garcia, M.O. (2015a) Cracking the olivine zoning code: Distinguishing between crystal growth and diffusion. Geology, 43, 935-938. https://doi.org/10.1130/G37082.1

Shea, T., Costa, F., Krimer, D., and Hammer, J.E. (2015b) Accuracy of timescales retrieved from diffusion modeling in olivine: A 3D perspective. American Mineralogist, 100, 2026-2042. https://doi.org/10.2138/am-2015-5163

Spera, F.J. (1984) Carbon dioxide and petrogenesis III: role of volatiles in the ascent of alkaline magma with special reference to xenolith-bearing magmas. Contributions to Mineralogy and Petrology, 88, 217-232.

Stalder, R., and Behrens, H. (2006) D/H exchange in pure and Cr-doped enstatite: implications for hydrogen diffusivity. Physics and Chemistry of Minerals, 33, 601-611. https://doi.org/10.1007/s00269-006-0112-z

Stalder, R., and Skogby, H. (2003) Hydrogen diffusion in natural and synthetic orthopyroxene: Physics and Chemistry of Minerals, 30, 12-19. https://doi.org/10.1007/s00269-002-0285-z

Sundvall, R., Skogby, H., and Stalder, R. (2009) Hydrogen diffusion in synthetic Fe-free diopside. European Journal of Mineralogy, 21, 963-970. https://doi.org/10.1127/0935-1221/2009/0021-1971

Tabor, F.A., Tabor, B.E., and Downes, H. (2010) Quantitative characterization of textures in mantle spinel peridotite xenoliths. Geological Society of London Special Publications, 337, 195-211. https://doi.org/10.1144/SP337.10

Thoraval, C., Demouchy, S., and Padrón-Navarta, J. A. (2018) Relative diffusivities of hydrous defects from a partially dehydrated natural olivine. Physics and Chemistry of Minerals, 46, 1-13. https://doi.org/10.1007/s00269-018-0982-x

Thoraval, C., and Demouchy, S. (2014) Numerical models of ionic diffusion in one and three dimensions: applications to dehydration of mantle olivine. Physics and Chemistry of Minerals, 41, 709-723. https://doi.org/10.1007/s00269-014-0685-x

Tian, Z-Z., Liu, J., Xia, Q-K., Ingrin, J., Hao, Y.T., and Christophe, D. (2017) Water concentration profiles in natural mantle orthopyroxenes: A geochronometer for long annealing of xenoliths within magma. Geology, 45, 87-90. https://doi.org/10.1130/G38620.1

Tollan, P.M.E., O'Neill, H.S.C., and Hermann, J. (2018) The role of trace elements in controlling H incorporation in San Carlos olivine. Contributions to Mineralogy and Petrology, 173, 89. https://doi.org/10.1007/s00410-018-1517-7.

Tollan, P.M.E., Dale, C.W., Hermann, J., Davidson, J.P., and Arculus, R.J. (2017) Generation and modification of the mantle wedge and lithosphere beneath the West Bismarck Island Arc: Melting, metasomatism, and thermal history of peridotite xenoliths from Ritter Island. Journal of Petrology, 58, 1475-1510. doi: 10.1093/petrology/egx062

Ulmer, P., and Trommsdorff, V. (1995) Serpentine stability to mantle depths and subduction-related magmatism. Science, 268, 858-861. https://doi.org/10.1126/science.268.5212.858

Van Orman, J.A., Grove, T.L., and Shimizu, N. (2001) Rare earth element diffusion in diopside: influence of temperature, pressure, and ionic radius, and an elastic model for diffusion in silicates. Contributions to Mineralogy and Petrology, 141, 687-703. https://doi.org/10.1007/s004100100269

Viccaro, M., Guiffrida, M., Zuccarello, F., Scandura, M., Palano, M., and Gresta, S. (2019) Violent paroxysmal activity drives self-feeding magma replenishment at Mt. Etna. Scientific Reports, 9, 6717. https://doi.org/10.1038/s41598-019-43211-9

Warren, J.M., and Hauri, E.H. (2014) Pyroxenes as tracers of mantle water variations. Journal of Geophysical Research: Solid Earth, 119, 1851-1881. https://doi.org/10.1002/2013JB010328

Warren, J.M., and Shimizu, N. (2010) Cryptic variations in abyssal peridotite compositions: Evidence for shallow-level melt infiltration in the oceanic lithosphere. Journal of Petrology, 51, 1-2, 395-423. https://doi.org/10.1093/petrology/egp096

Warren, J.M., Shimizu, N., Sakaguchi, C., Dick, H.J.B., and Nakamura, E. (2009) An assessment of upper mantle heterogeneity based on abyssal peridotite isotopic compositions. Journal of Geophysical Research, 114, B12203. https://doi.org/10.1029JB006186

Wegner, W.W., and Ernst, W.G. (1983) Experimentally determined hydration and dehydration reaction rates in the system MgO-SiO_2-H_2O. American Journal of Science, 283-A, 151-180.

Woods, S.C., Mackwell, S., and Dyar, D. (2000) Hydrogen in Diopside: Diffusion profiles. American Mineralogist, 85, 480-487. https://doi.org/10.2138/am-2000-0409

Workman, R.K., and Hart, S.R. (2005) Major and trace element composition of the depleted MORB mantle (DMM). Earth and Planetary Science Letters, 231, 53-72. https://doi.org/10.1016/j.epsl.2004.12.005

Xu, Y., Tang, W., Hui, H., Rudnick, R.L., Shang, S., and Zhang, Z. (2019) Reconciling the discrepancy between the dehydration rates in mantle olivine and pyroxene during xenolith emplacement. Geochimica et Cosmochimica Acta, 267, 179-195. doi: 10.1016/j.gca.2019.09.023

Yang, Y., Ingrin, J., Xia, Q., and Liu, W. (2019) Nature of hydrogen defects in clinopyroxenes for room temperature up to 1000ºC: Implication for the preservation of hydrogen in the upper mantle and impact on electrical conductivity. American Mineralogist, 104, 79-93. https://doi.org/10.2138/am-2019-6661

Zhang, Y. (2010) Diffusion in minerals and melts: Theoretical background. Reviews in Mineralogy and Geochemistry, 72, 5-59. https://doi.org/10.2138/rmg.2010.72.2

Table 1: Summary of model conditions and resolution.

Mineral Phase	**$Kd_{H2O}^{min/melt}$[1]**	**C_0 (ppm)[2]**	**C_1 low-H (ppm)[3]**	**1 or 2% error (±ppm)[4]**	**10% error (±ppm)[5]**	**1 or 2% effective re-eq.[6]**	**10% effective re-eq.[7]**	**C_1 high-H (ppm)[8]**	**1 or 2% error (± ppm)**	**10% error (± ppm)**	**1 or 2% effective re-eq**	**10% effective re-eq.**
Ol	0.002	7	15	0.3	1.5	96	81	32	0.6	3.2	98	87
Opx	0.018	50	135	1.4	14	98	84	300	3	30	99	88
Cpx	0.047	200	353	3.5	35	97	77	750	7.5	75	99	86
Cpx*	-	200	1000	-	-	-	-	10000	-	-	-	-

Note(s): Cpx* indicates additional models run at 800ºC to test hydrothermal boundary conditions. [1] Internally consistent mineral-melt partition coefficients from Warren and Hauri (2014) used to calculate boundary conditions for models in equilibrium with partial melt. [2] Initial core compositions prior to diffusion, taken from the low end of the range of calculated upper mantle values in Hirschmann (2006) and Warren and Hauri (2014). [3] Low-H boundary condition, constrained by partition coefficients and mid-ocean ridge basalt with 0.75 wt% H_2O. [4] Typical error on high precision analyses – 1% for opx and cpx and 2% for olivine (see Supplementary Material for derivation). [5] Representative error for "poor" analytical measurements (see Supplementary Material). [6] Effective percent re-equilibration for 1% (pyx) or 2% (ol) error on low-H model boundary conditions, at which diffusion profiles are not resolvable within analytical error. [7] Effective percent re-equilibration for 10% error on low-H model boundary conditions. [8] High-H boundary condition, constrained by the high end of the range of upper mantle values (Hirschmann 2006; Warren and Hauri 2014).

Table 2: Modeled 100% re-equilibration timescales for 1 and 3 mm minerals with upper and lower bounds of uncertainty from Figure 4.

Mineral	**T(°C)**	**100% re-eq time (1 mm)**			**100% re-eq time (3 mm)**		
		upper	**model**	**lower**	**upper**	**model**	**lower**
Cpx PP	600	1 day	14 days	63 days	6 days	55 days	84 days
	700	12 hrs	1 days	3 days	3 days	8 days	17 days
	800	2 hrs	4.5 hrs	5 hrs	10 hrs	19 hrs	24 hrs
	1000	2 mins	12 mins	14 mins	11 mins	1 hr	1.5 hrs
	1200	4 sec	1.5 mins	2 mins	30 sec	7 mins	12 mins
Opx PP	600	60 days	1.4 yrs	200 yrs	1 yr	6.5 yrs	1500 yrs
	700	8 days	25 days	1.6 yrs	60 days	175 days	10.5 yrs
	800	14 hrs	2 days	23 days	3.5 days	13.5 days	166 days
	1000	2 mins	72 mins	3 days	10 mins	7.5 hrs	17 days
	1200	0.7 sec	5 mins	20 hrs	4 sec	30 mins	5 days
Ol PP	600	5 hrs	4 days	18 days	3 days	24 days	120 days
	700	6 hrs	20 hrs	2.9 days	2 days	5 days	18 days
	800	2 hrs	4 hrs	6 hrs	18 hrs	23 hrs	2 days
	1000	14 mins	26 mins	45 mins	1.9 hrs	2 hrs	6 hrs
	1200	2 mins	4 mins	17 mins	12 mins	27 mins	2 hrs
Ol PV	600	25 hrs	160 yrs	230 yrs	25 hrs	1300 yrs	1605 yrs
	700	9.6 hrs	4.9 yrs	16.2 yrs	3 days	39 yrs	65 yrs
	800	1 day	128 days	264 days	7 days	5 yrs	8 yrs
	1000	16 hrs	4 days	5.7 days	5 days	20 days	51 days
	1200	48 mins	4 hrs	10 days	7 hrs	22 hrs	75 days
Ol tot	600	4 hrs	76 days	230 days	1 day	1 yr	5 yrs
	700	11 hrs	12 days	21 days	3 days	74 days	135 days
	800	12 hrs	2 days	3 days	2 days	14 days	15 days
	1000	1 hr	6 hrs	2 days	7 hrs	1.5 days	10.5 days
	1200	5 mins	1.5 hrs	3 days	31 mins	7 hrs	27 days

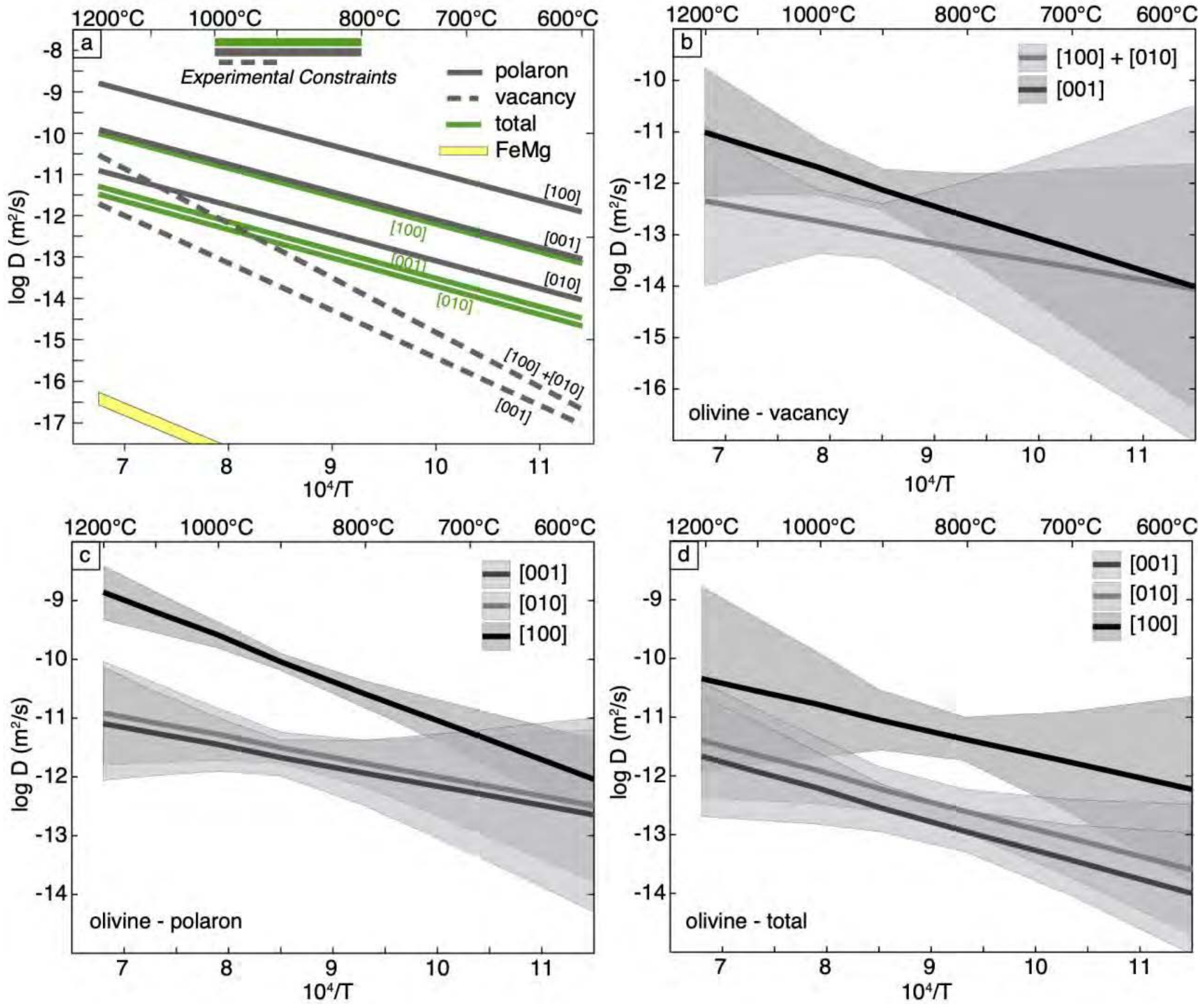

Figure 1: Arrhenius diagram showing H$^+$ diffusion rates in olivine for the proton polaron mechanism (solid grey lines - Mackwell and Kohlstedt 1990), proton vacancy mechanism (dashed grey lines - Demouchy and Mackwell 2006), and total H$^+$ diffusion (green lines - Ferriss et al. 2018). Olivine D$_{\mathrm{FeMg}}$ (yellow region) is shown for comparison (Dohmen and Chakraborty 2007a, 2007b). Anisotropic diffusivities are labeled for each principal crystallographic axes. Experimental constraints between 800-1000°C (shown at the top of the figure) were used to extrapolate using the log-linear Arrhenius relationships. Uncertainties associated with this extrapolation are represented by 95% confidence interval error envelopes (shaded fields) calculated from experimental data for the (b) proton vacancy mechanism, (c) proton polaron mechanism, and (d) "total" H diffusion.

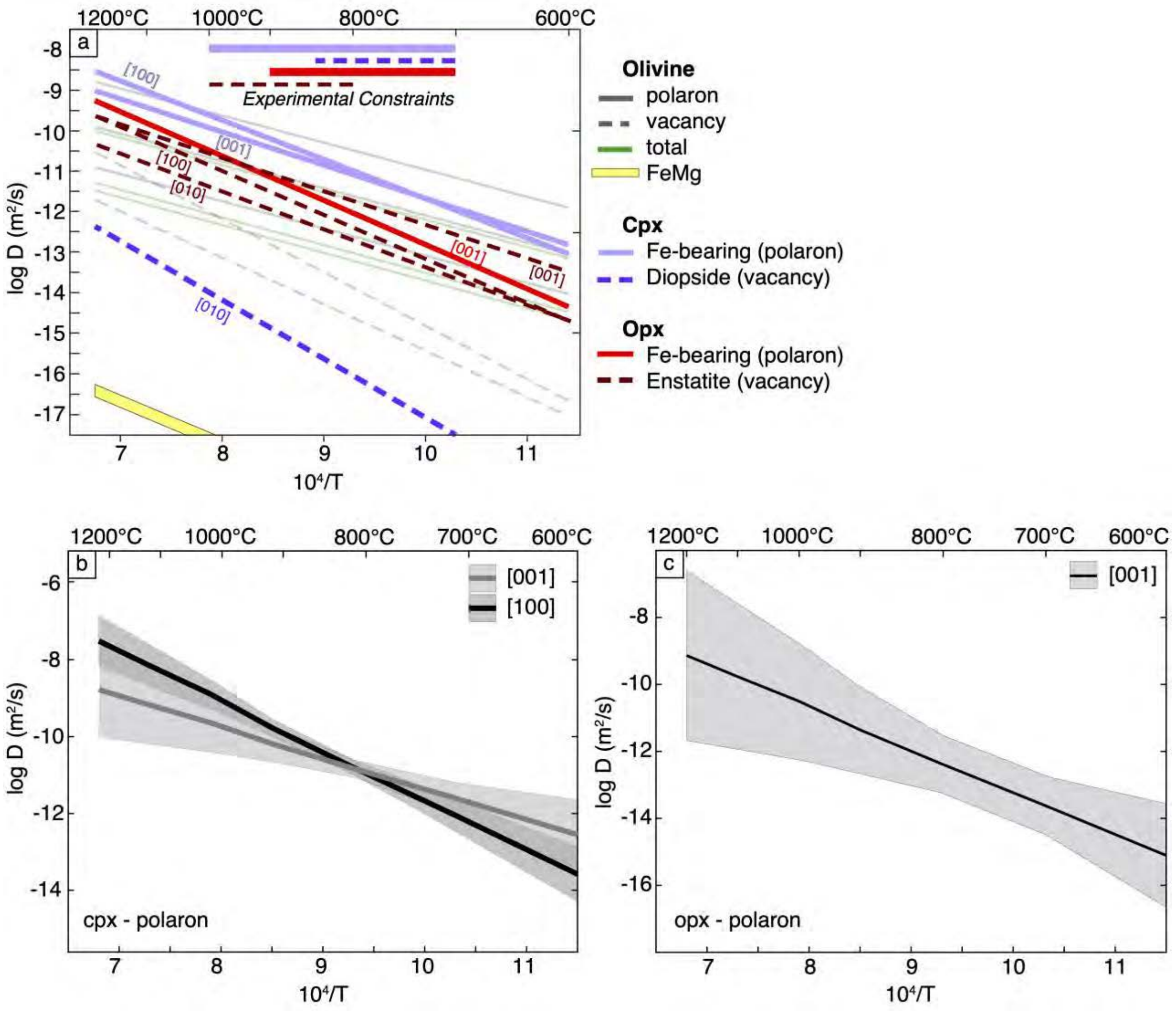

Figure 2: (a) Arrhenius diagram showing H^+ diffusion rates in clinopyroxene (Jaipur diopside for the proton-polaron mechanism, Woods et al. 2000; Ferriss et al. 2016 and synthetic diopside for the proton vacancy mechanism, Sundvall et al. 2009) and orthopyroxene (Kilbourne Hole enstatite for the proton-polaron mechanism, Stalder and Skogby 2003 and synthetic enstatite for the proton-vacancy mechanism, Stalder and Behrens 2006) overlaid on the olivine mechanisms (Mackwell and Kohlstedt 1990; Demouchy and Mackwell 2006; Ferriss et al. 2018). Olivine D_{FeMg} is shown for comparison (Dohmen and Chakraborty 2007a, 2007b). Isotropic data (or experimental datasets where only one crystallographic axis has an Arrhenius relationship constrained) have one line, while anisotropic diffusivities have multiple lines for different crystallographic axes. Experimental constraints between 700-1000°C (shown at the top of the figure) were used to extrapolate using the log-linear Arrhenius relationships. (b) Clinopyroxene proton-polaron and (c) orthopyroxene proton-polaron Arrhenius relationships are shown with 95% confidence interval error envelopes (shaded fields) calculated from experimental data.

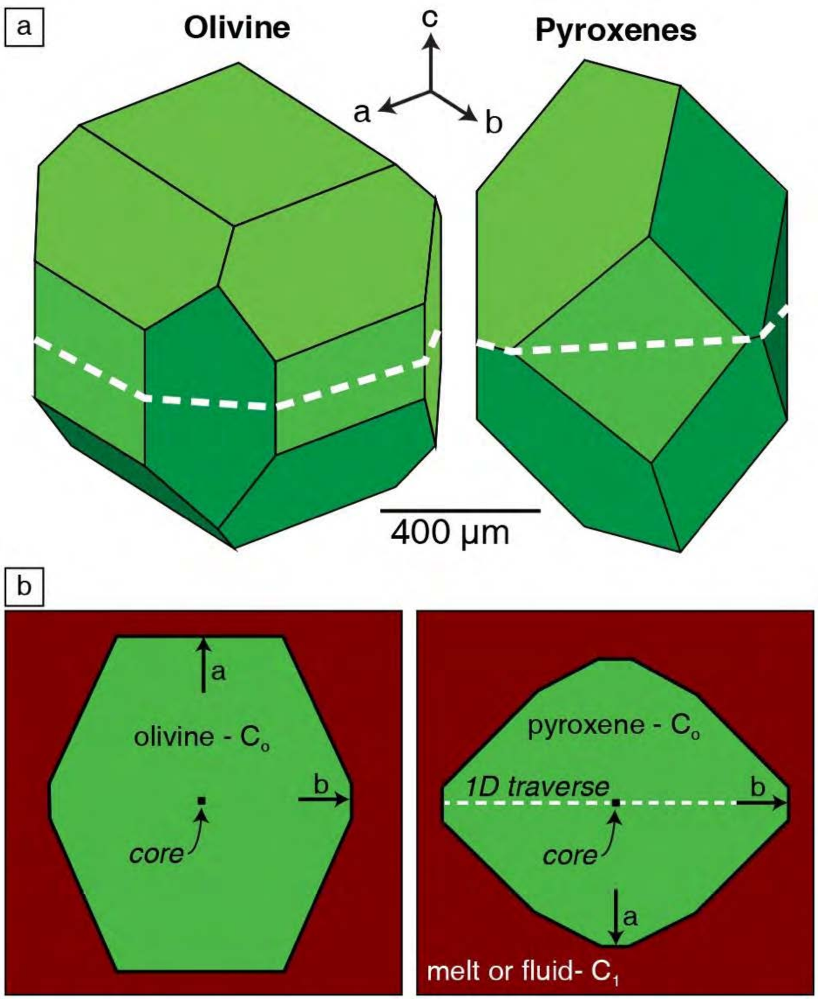

Figure 3: (a) Single-crystal 3D models used to examine diffusive re-equilibration of H in olivine and pyroxenes. (b) 2D sections perpendicular to the c-axis through the core of the crystal (white line in *a*). The H concentration of the black core pixel labeled “core” (a voxel in 3D) is sampled at regular intervals throughout the diffusion models to track % re-equilibration. The white dashed line is the location of the 1D clinopyroxene traverse, sampled parallel to the *b*-axis.

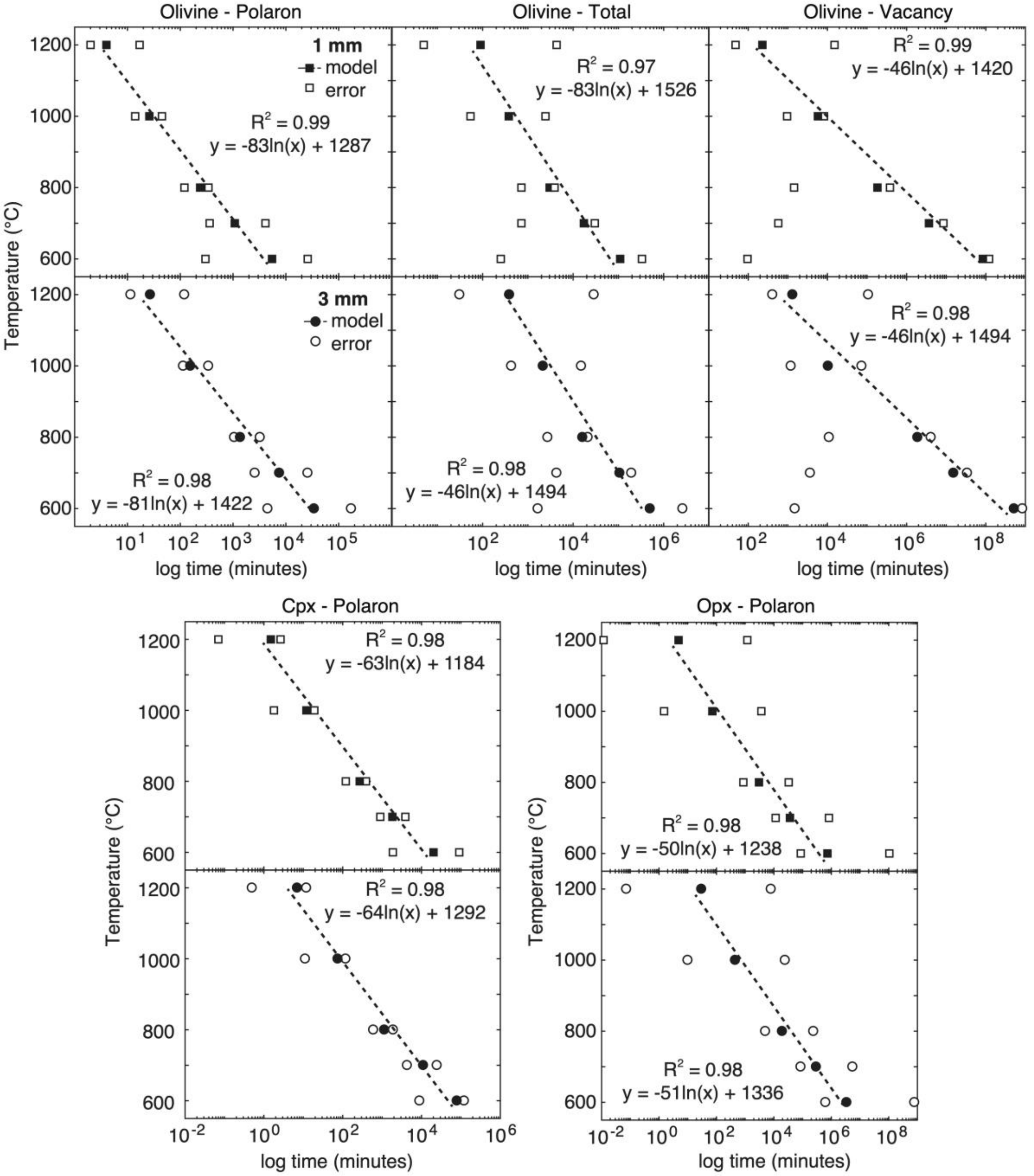

Figure 4: The relationship between temperature and 100% re-equilibration timescale, including the effect of diffusion coefficient uncertainties for model timescales. Results reflect both low-H and high-H models, as the 100% re-equilibration timescales are insensitive to the choice of boundary condition. The 100% re-equilibration timescales have strong log-linear trends as a function of temperature (R^2 from 0.97 to 0.99) that can be used to calculate expected re-equilibration time at a given temperature and grain size. The errors in the models (white symbols) are determined by using the uncertainty range for the diffusion coefficients (Figures 1-2). Uncertainties are greatest for the olivine proton vacancy (PV) models, for which experimental data covers a limited temperature range (900-1000°C).

Correction 08/21/20

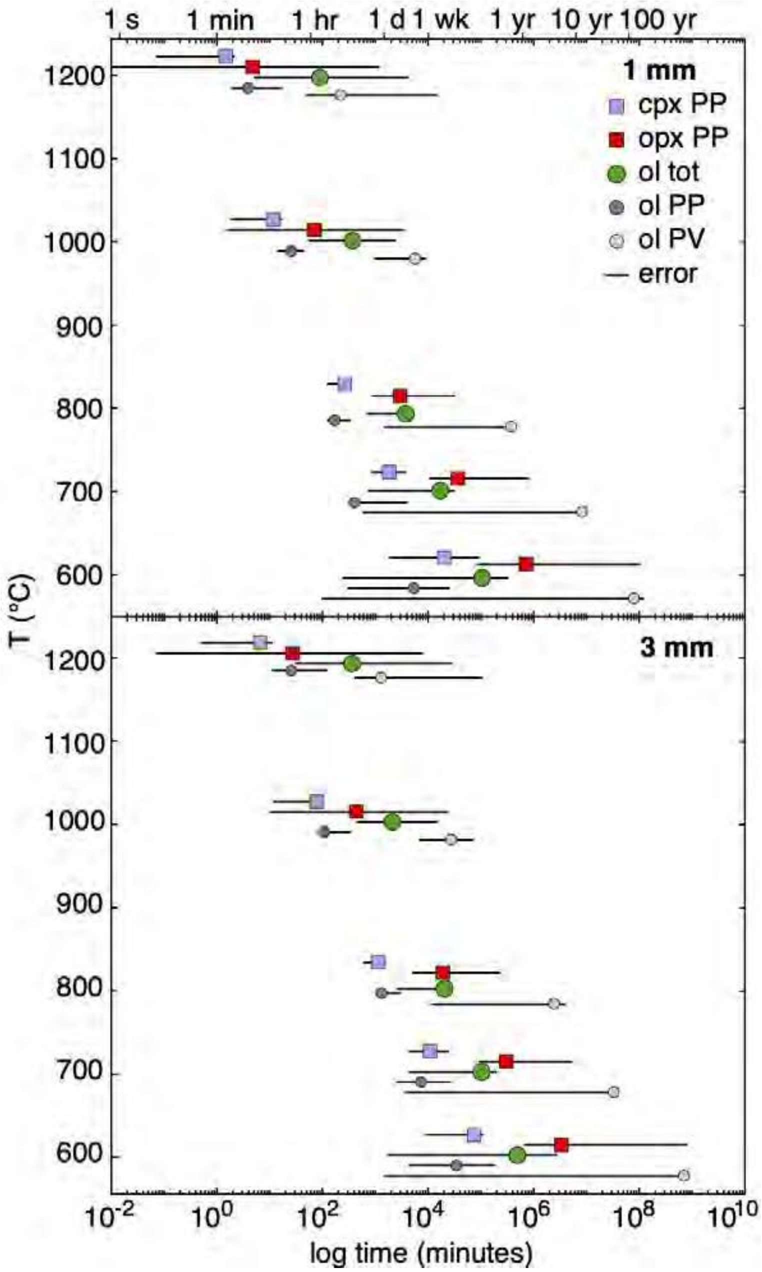

Figure 5: Modeled diffusion durations (log time, minutes) for 100% re-equilibration of 1 mm and 3 mm grains from 600-1000°C. Results reflect both low-H and high-H models, as the 100% re-equilibration timescales are insensitive to the choice of boundary condition. Clinopyroxene (purple squares) and orthopyroxene (red squares) proton-polaron models utilize Fe-bearing diffusivities (Woods et al. 2000; Ferriss et al. 2016; Stalder and Skogby 2003). Three olivine models are shown: the fast proton polaron mechanism (ol PP, dark grey circles; Mackwell and Kohlstedt 1990), the slower proton vacancy mechanism (ol PV, light grey circles; Demouchy and Mackwell 2006), and the intermediate total H^+ diffusion expression (ol tot, green circles; Ferriss et al. 2018). Upper and lower bounds of error envelopes calculated for experimental data are represented by the lines and reflect the potential uncertainty in the modeled re-equilibration timescale.

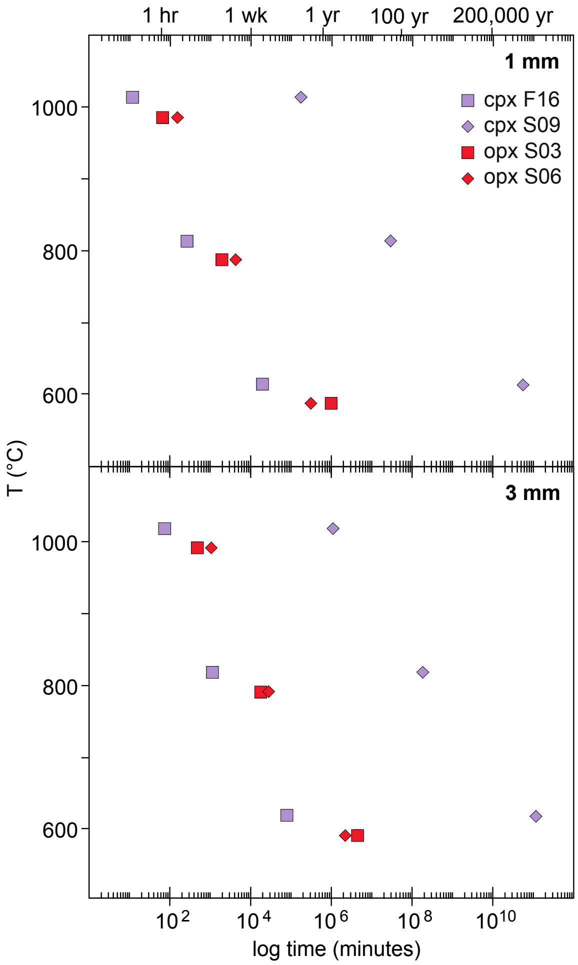

Figure 6: Model results for proton-polaron diffusion mechanisms (squares) compared to possible proton-vacancy diffusion mechanisms (diamonds) for 1 and 3 mm pyroxene models. Proton-polaron models (square symbols) are as shown in Figure 5. Models representing the proton-vacancy mechanism utilize Sundvall et al. (2009; purple diamonds) for cpx and Stalder and Behrens (2006; red symbols) for opx. Legend abbreviations are: F16 – Ferriss et al. 2016; S09 – Sundvall et al. 2009; S03 – Stalder and Skogby 2003; S06 – Stalder and Behrens 2006.

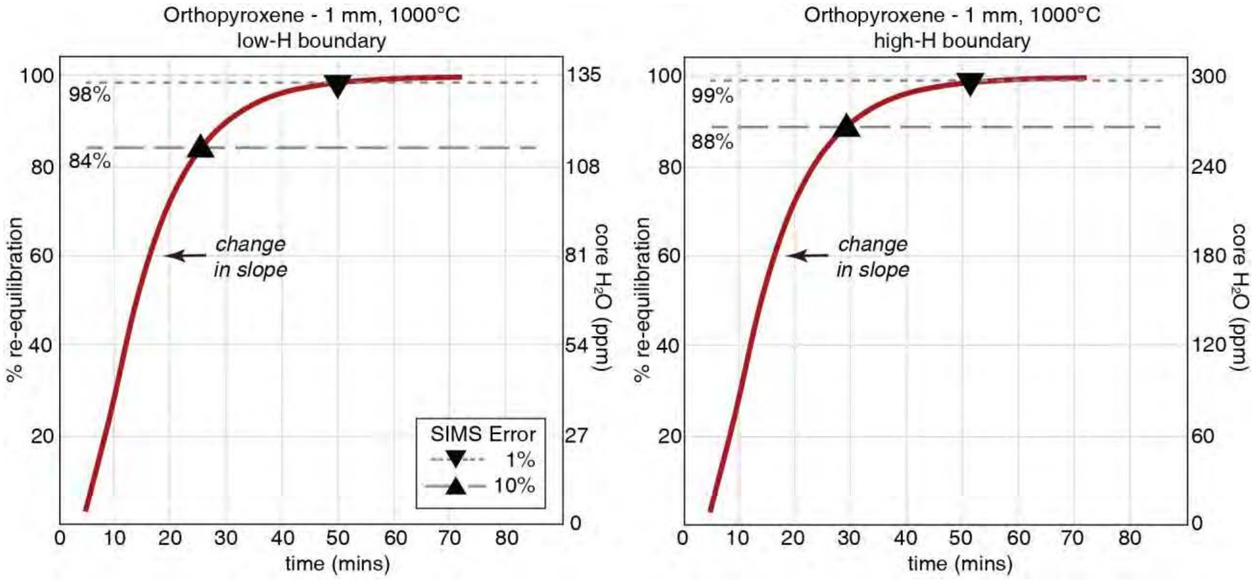

Figure 7: Orthopyroxene re-equilibration with diffusion time for the low-H (left) and high-H (right) boundary conditions using the proton-polaron diffusion coefficient. Black downward pointing triangles (1% analytical error) and upward-pointing triangles (10% analytical error) indicate the effective %re-equilibration point for each model, where any zonation beyond that value would be difficult to resolve outside of analytical error. For the low-H boundary, 1% analytical error intersects the modeled re-equilibration line after 50 minutes of diffusion, which is a 30% shorter duration compared to the 100% re-equilibration time of 72 minutes (Table 2). The 10% error intersects the re-equilibration line after ~25 minutes, representing a duration that is about 65% shorter compared to the 100% time. For the high-H boundary, 1% error intersects the modeled re-equilibration line after ~52 minutes, and 10% error intersects at ~28 minutes (Supplementary Table S4).

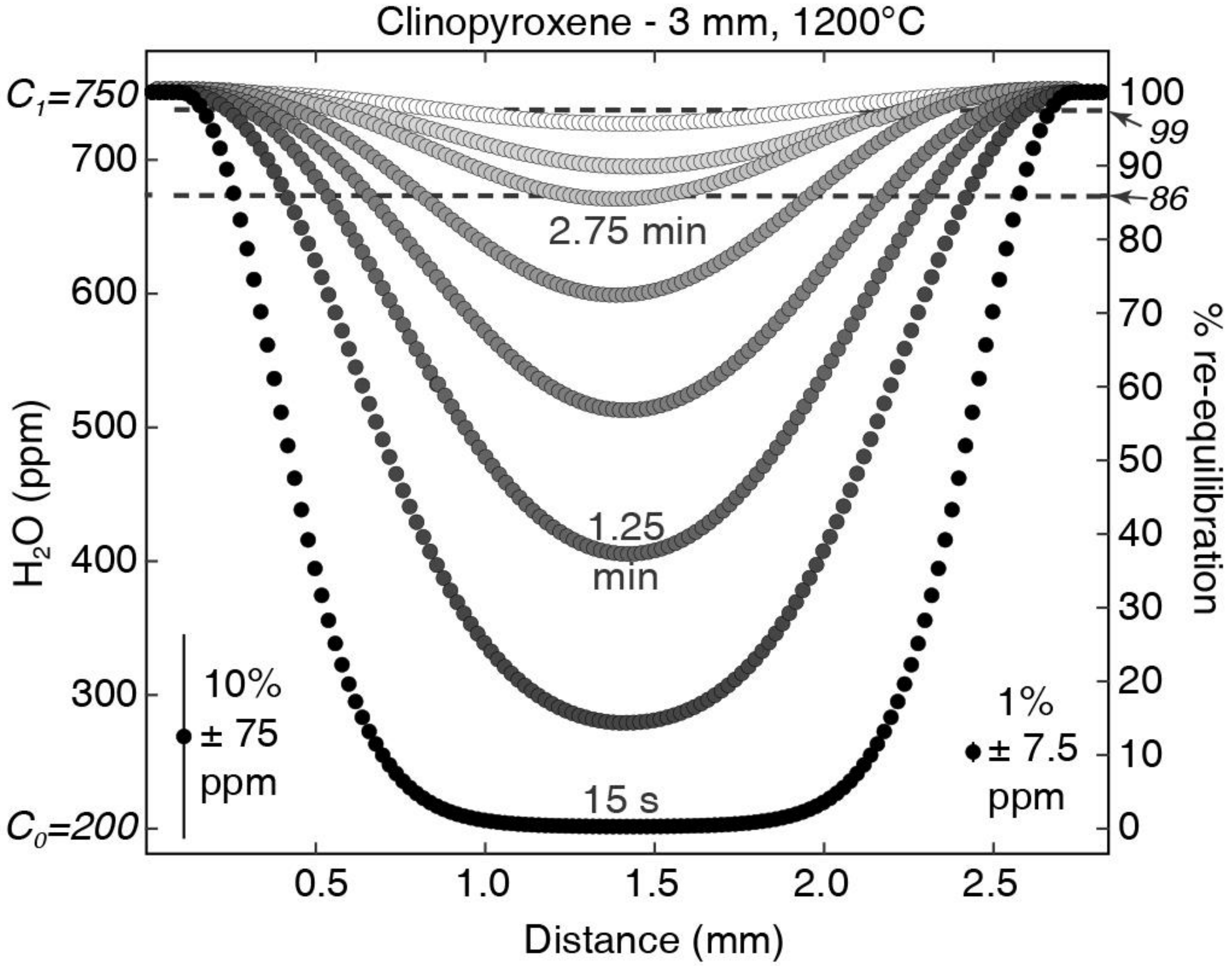

Figure 8: 1D transects with diffusion time from the cpx proton-polaron high-H boundary condition model for a 3 mm diameter grain at 1200°C. These 1D traverses were extracted parallel to the *b*-axis in the ideal 2D section shown in Figure 3. After only 1.25 minutes of diffusion, the core composition shows a factor of two increase in water content and is 40% re-equilibrated with the boundary condition. After ~3 minutes, the core concentration has reached 99% re-equilibration which is the effective % re-equilibration (indicated by the dashed line at *99)* where distinguishing zoning profiles between the core and rim of the crystal becomes difficult due to error on typical NAM water measurements (see discussion in Supplementary Material). If analytical precision is even poorer (e.g., 10% error), analyses are only resolvable until 86% re-equilibration (dashed line at 86). For this high-H boundary condition, the 1% uncertainty is 7.5 ppm and the 10% uncertainty is 75 ppm (Table 1).

Supplementary Material for:

The potential for aqueous fluid-rock and silicate melt-rock interactions to re-equilibrate hydrogen in peridotite nominally anhydrous minerals

Kendra J. Lynn (kjlynn@udel.edu) and Jessica M. Warren

Numerical Model Setup

Our models utilize recent advances in numerical diffusion approaches that address diffusion anisotropy by allowing for high resolution investigation of diffusing species in three dimensions (c.f., Shea et al. 2015a, 2015b; Lynn et al. 2017; Krimer and Costa 2017; Jollands and Müntener 2019; Mutch et al. 2019). Previous studies have used the slowest and/or fastest crystal directions to provide maximum or minimum timescale estimates when modeling in one dimension (1D; e.g., Pan and Batiza 2002; Longpré et al. 2014; Thoraval and Demouchy 2014). However, three-dimensional modeling of compositional zoning in olivine by Shea et al. (2015b) showed that this approach results in timescales that are up to 25x longer than the true diffusion time. They advocated for a 3D volume diffusion approach that fully treats diffusion anisotropy.

The numerical models have dimensions of 221 x 221 x 221 voxels, representing olivine or pyroxene surrounded by silicate melt or aqueous fluid (Figure 3 in the main text). Different voxel sizes allowed us to test two mineral grain sizes. Voxels with a resolution of 4 x 4 x 4 µm yielded crystals that are ~1 mm along the *c*-axis and voxels of 20 x 20 x 20 µm yielded crystals that are ~3 mm along the *c*-axis.

Diffusion within the crystal volume was simulated in Matlab using finite differences and the non-concentration dependent three-dimensional form of Fick's second law (Crank 1975). This form assumes that diffusion coefficients are not sensitive to the concentration of H^+ or other elements. For isotropic calculations (e.g., as simplified for opx, for which only the [001] Arrhenius relationship is constrained), it has the form:

$$\frac{\partial C}{\partial t}=D\left[\frac{\partial^2 C}{\partial x^2}+\frac{\partial^2 C}{\partial y^2}+\frac{\partial^2 C}{\partial z^2}\right] \qquad (1)$$

where *C* is the hydrogen concentration expressed in ppm H_2O, *t* (s) is time, *D* (m^2/s) is the diffusion coefficient for H, and *x, y*, and *z* are spatial dimensions along Cartesian coordinates. The full numerical expressions for implementation of the models can be found in the Supplementary material of Shea et al. (2015b).

For simplicity, all numerical models are for orthorhombic crystals, where the diffusivity tensor with axes *a*, *b*, and *c* takes the form

$$D=\begin{bmatrix} D_a & 0 & 0 \\ 0 & D_b & 0 \\ 0 & 0 & D_c \end{bmatrix} \tag{2}$$

where $D_a=D_x$, $D_b=D_y$, and $D_c=D_z$ (Zhang, 2010). Modeling anisotropic diffusion (cpx and olivine) requires the following non-concentration dependent 3D form of Fick's second law:

$$\frac{\partial C}{\partial t}=\left[D_a\frac{\partial^2 C}{\partial x^2}+D_b\frac{\partial^2 C}{\partial y^2}+D_c\frac{\partial^2 C}{\partial z^2}\right] \tag{3}$$

where D_a, D_b, and D_c are the different diffusivities along the *a*-, *b*-, and *c*-axes, respectively. Comparison of cpx and opx sections in Figure S1 demonstrates the effects of anisotropic vs. isotropic diffusion.

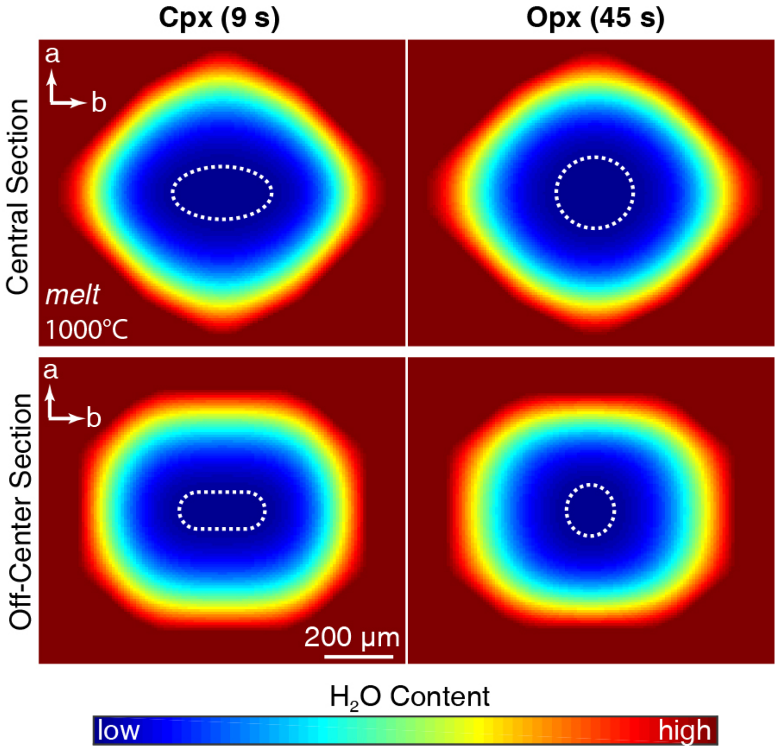

Figure S1: Examples of pyroxene models with anisotropic (Fe-bearing cpx; Woods et al. 2010; Ferriss et al. 2016) and isotropic (Fe-bearing opx with only an Arrhenius relationship for [001]; Stalder and Skogby 2003) diffusion behavior. Zonation of H_2O is scaled with color. The dashed white line represents the diffusion front, where the area inside the white line is the homogeneous core composition.

Models were initially run for two sets of boundary conditions, both of which correspond to NAM water contents in equilibrium with silicate melts outside the crystal. The "low-H" models have boundary conditions that were calculated using mineral-melt partition coefficients from Warren and Hauri (2014) and are in equilibrium with a basaltic partial melt that has 0.75 wt% H_2O. Boundary values are 15 ppm for olivine, 135 ppm for opx, and 353 ppm for cpx (Table 1). The "high-H" models were run with the boundary condition set to the high end of the estimated water content range for each mineral in the upper mantle. Boundary values are 32 ppm for olivine, 300 ppm for opx, and 750 ppm for cpx (Hirschmann 2006; Warren and Hauri 2014). These maximum water contents correspond to a melt H_2O content of ~1.6 wt%, slightly above the range for mid-ocean ridge basalt (0.5 – 1.2 wt% H_2O; Ligi et al. 2005; Le Voyer et al. 2015; Li et al. 2017). These models allow us to evaluate the timescales over which silicate melt-rock interactions can give rise to water contents in NAMs that look similar to inferred mantle abundances.

An additional subset of cpx models was run at 800°C with higher boundary conditions to assess the sensitivity of the models to the choice of boundary condition. The experimentally determined H_2O solubility/storage capacity of NAMs varies widely with pressure, temperature, and mineral chemistry (e.g., Kohlstedt et al. 1996; Woods et al. 2000; Rauch and Keppler 2002; Stalder and Skogby 2002; Bromiley et al. 2004; Mierdel and Keppler 2004; Zhao et al. 2004; Hirschmann et al. 2005; Keppler and Bolfan-Casanova 2006; Withers and Hirschman 2008; Bali et al. 2008; Withers et al. 2011; Ferot and Bolfan-Casanova 2012; Ardia et al. 2012; Tenner et al. 2012; Demouchy and Bolfan-Casanova 2016). Most of these experiments don't include NAMs with natural mantle compositions or were conducted at pressures or temperatures too high for lithospheric conditions, thus limiting the application of solubility constraints to our determination of aqueous fluid boundary conditions here. We therefore implemented hypothetical boundary values of 10^3 and 10^4 ppm H_2O to provide an upper bound on hydrothermal fluid boundary conditions for the additional cpx models.

We track the longest possible duration that a 1-3 mm diameter grain can preserve its initial (e.g., mantle inherited) water content by sampling the central voxel of the 3D models. Most natural samples have crystal sections that are highly off-center and oblique (Figure S2), so tracking the H^+ content at the central voxel yields the most conservative estimates of re-equilibration timescales. This conservative estimate is useful for understanding the resiliency of a diffusing species to overprinting by later processes. However, non-ideal sections (i.e. off-center and oblique) of natural minerals would reflect greater degrees of re-equilibration more quickly than predicted by the core voxel (Shea et al. 2015b; Lynn et al. 2017).

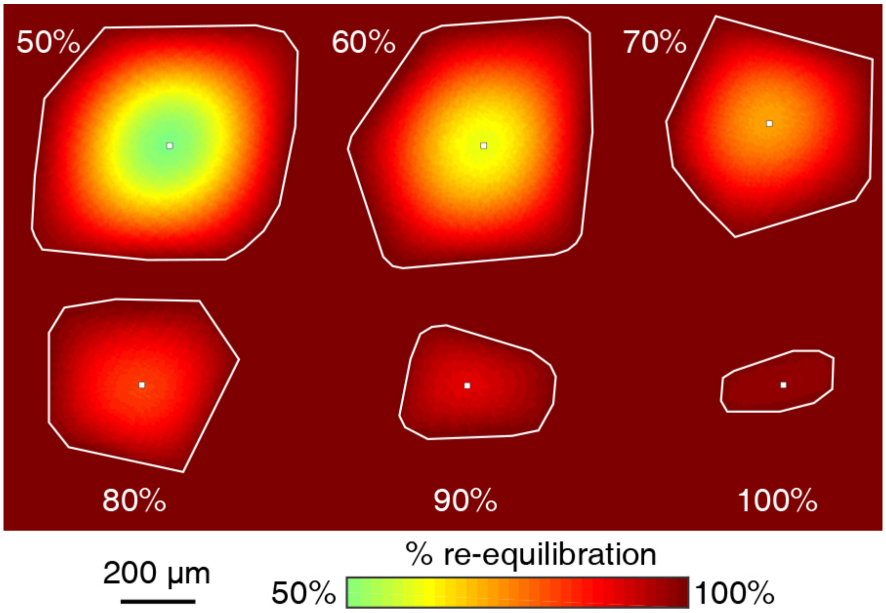

Figure S2: Numerical "thin section" of orthopyroxene slices (white outlines) taken at random orientations and distances away from the crystal core. The red background represents the boundary condition (e.g., surrounding fluid or melt). The opx crystal used for this example was taken from the high-H boundary condition model for a 1 mm diameter grain at 1000°C after 13.5 minutes of diffusive re-equilibration. The core composition was 173 ppm H_2O for the central pixel (~50% re-equilibrated). The color bar represents the compositional gradient induced by diffusion shown as % re-equilibration. The % re-equilibration sampled at the central pixel (white square) is labeled next to each slice. The 50% example is a near-ideal slice through the crystal's core, whereas the 100% example is highly off-center.

Effective %Re-equilibration

Numerical models have essentially unrestricted compositional resolution, the analytical precision of measurements in natural samples must be considered when interpreting our re-equilibration timescales as bounds on the kinetic window of hydrogen. The two main techniques for measuring H^+ in NAMs are secondary ion mass spectrometry (SIMS) and Fourier transform infrared spectroscopy (FTIR). SIMS analytical techniques and calibrations have advanced significantly in recent decades, particularly with improved methods for minimizing background water (e.g., only a few ppm) and for propagating errors (e.g., Hauri et al. 2002; Aubaud et al.

2007; Kumamoto et al. 2017). Measurements using FTIR offer the benefit of site-specific distributions of H^+ storage and diffusion pathways, but analytical resolution depends on the choice of polarized vs. unpolarized measurements, oriented vs. unoriented grains, and sample thickness (e.g., Bell et al. 2003; Aubaud et al. 2009; Stalder et al. 2012; Mosenfelder and Rossman 2013a, 2013b; Withers et al. 2012). For abyssal, opholitic, and orogenic peridotites, NAM water contents are more commonly measured by SIMS (e.g., Gose et al. 2009; Peslier 2010; Schmädicke et al. 2011; Warren and Hauri 2014; Kumamoto et al. 2019). Thus, we utilize the analytical uncertainty from Warren and Hauri (2014) for SIMS measurements of olivine, opx, and cpx to adjust our modeled 100% re-equilibration timescales.

Individual 1D profiles of H zoning measured by SIMS may be modeled using the measured count per second ratio of $^{17}OH/^{30}Si$ or $^{1}H/^{16}O$. The additional uncertainties associated with converting count ratios to absolute concentrations can be avoided as H^+ diffusion coefficients are non-concentration dependent. The point-to-point precision of the analytical routine can be estimated from the count statistic error associated with each SIMS analysis, which is calculated from the Poisson distribution of the five-cycle count ratio average. The average count statistic error of olivine analyses in Warren and Hauri (2014) is 2 ± 1% (n=73 analyses), whereas pyroxenes are 1 ± 1% (n=250). While these count uncertainties may be small in absolute terms, they have a significant effect on our modeled timescales. Thus, we calculated an effective %re-equilibration to evaluate the resolvable re-equilibration timescales in natural samples. This parameter is calculated following Eq. 4, with the $H_{equilibrium}$ value for the boundary condition adjusted to reflect analytical uncertainties. A second effective %re-equilibration is calculated using 10% analytical error, chosen to represent reduced SIMS precision due to issues such as machine instability or variable backgrounds.

For olivine, the 2% uncertainty equates to a reduction in the resolvable boundary concentration by 0.3 and 0.6 ppm for low-H and high-H boundary conditions. This yields effective boundaries of 14.7 and 31.4 ppm, respectively, representing 96.3% and 97.6% re-equilibration (Figure S3). 10% uncertainties for the low-H and high-H boundary conditions correspond to a reduction of 1.5 and 3 ppm in resolvable boundary concentrations. This yields an effective re-equilibrated composition of 13.5 ppm H_2O or only 81% of the total % re-equilibration in our models with the low boundary condition (Figure S3). The real model diffusion time for the 1 mm olivine "total" D_H (Ferriss et al. 2018) at 1000ºC is ~6 hours, but the effective re-equilibration time at 10% uncertainty is only ~2 hours (Table S1).

For cpx, 1% SIMS uncertainty equates to a reduction in the resolvable boundary concentration by 3.5 and 7.5 ppm for the low-H and high-H boundary conditions, respectively. The effective boundary conditions become 349 and 742 ppm, corresponding to 97% and 99% re-equilibration (Table 1 in the main text). The 10% uncertainty in count statistics translates to 35 and 75 ppm for low-H and high-H boundary conditions, with the effective boundary conditions at 315 and 675 ppm. This corresponds to 77% and 86% of the total re-equilibration determined by our low-H and high-H models, respectively (Table 1 in the main text).

For opx, an analytical error of 1% equates to a reduction in the resolvable boundary concentration by 1.4 ppm for the low-H models and 3 ppm for high-H boundary conditions. This results in effective boundaries of 133.6 and 297 ppm for low-H and high-H models, respectively, corresponding to 98.4 to 98.8% effective re-equilibration values (Table 1 in the main text, see also Table S5). At 1000 ºC for a 1 mm opx model (Figure 7 in the main text), ~98% re-equilibration corresponds to a model timescale of only 50 minutes compared to the 100% re-equilibration timescale of 72 minutes. When uncertainty in the opx water content is increased to 10%, the model uncertainty is 14 ppm for low-H and 30 ppm for high-H boundary conditions. This corresponds to 84% effective re-equilibration for the low boundary models and 88% for the high boundary models (Figure 7 in the main text). The modeled 1 mm opx timescale at 1000ºC is 72 minutes, but the effective timescales are ~25.5 minutes and ~28 minutes for the low-H and high-H silicate melt boundary conditions, respectively (see Supplementary Data File and Table S5).

Resolving diffusion profiles by SIMS or FTIR also requires good spatial resolution. In the case of SIMS, this may require that a reduced spot size is used, which will reduce the number of counts measured and thus increase analytical error. For FTIR, the spatial resolution depends both on detector setup and sample thickness (e.g., Gose et al. 2011). Hence, when spatial resolution is limited, the effective kinetic window for H re-equilibration in NAMs will similarly be reduced.

Table S5: Effective re-equilibration timescales for 1 and 3 mm minerals calculated using the low-H boundary conditions. The SIMS error timescales are calculated using 1% (cpx, opx) or 2% (ol) errors based on count statistics from measurements made by Warren and Hauri (2014). 100% re-eq timescales are the "model" columns from Table 2 in the main text for comparison. Effective timescales calculated using the high-H boundary conditions can be found in the Supplementary Data File in Table S4.

Mineral	**T(°C)**	**100% re-eq**		**1% (pyx) or 2% (ol) error**		**10% error**	
		1 mm	**3 mm**	**1 mm**	**3 mm**	**1 mm**	**3 mm**
Cpx PP	600	14 days	55 days	7.5 days	46 days	3.8 days	23 days
	700	1 days	8 days	17 hrs	4.4 days	8.2 hrs	2.3 days
	800	4.5 hrs	19 hrs	2.4 hrs	15 hrs	1.2 hrs	7.6 hrs
	1000	12 mins	1 hr	7.2 mins	46 mins	3.6 mins	23 mins
	1200	1.5 mins	7 mins	0.8 mins	5 mins	0.4 mins	2.5 mins
Opx PP	600	1.4 yrs	6.5 yrs	361 days	6 years	183 days	3 yrs
	700	25 days	175 days	18 days	111 days	9 days	53 days
	800	2 days	14 days	1.5 days	9.5 days	23 hrs	5 days
	1000	72 mins	7.5 hrs	52 mins	5.4 hrs	25 mins	2.8 hrs
	1200	5 mins	30 mins	3 mins	21 mins	1.7 mins	11 mins
Ol PP	600	4 days	24 days	3 days	18 days	1.4 days	8.5 days
	700	20 hrs	5 days	11 hrs	2.8 days	6.3 hrs	1.6 days
	800	4 hrs	23 hrs	2.4 hrs	15 hrs	70 mins	7.2 hrs
	1000	26 mins	2 hrs	14 mins	90 mins	7 mins	44 mins
	1200	4 mins	27 mins	2.6 mins	17 mins	1.4 mins	8.5 mins
Ol PV	600	160 yrs	1300 yrs	135 yrs	844 yrs	60 yrs	463 yrs
	700	4.9 yrs	39 yrs	9.5 yrs	37 yrs	6.2 yrs	24 yrs
	800	128 days	5 yrs	160 days	2.8 yrs	86 days	1.5 yrs
	1000	4 days	20 days	2.3 days	15 days	1.3 days	8 days
	1200	4 hrs	22 hrs	2.4 hrs	15 hrs	1.2 hrs	7.5 hrs
Ol tot	600	76 days	1 yr	44 days	274 days	22 days	134 days
	700	12 days	74 days	6.9 days	43 days	4 days	26 days
	800	2 days	14 days	1.6 days	9.8 days	19 hrs	4.8 days
	1000	6 hrs	1.5 days	3.7 hrs	23 hrs	1.9 hrs	12 hrs
	1200	1.5 hrs	7 hrs	43 mins	4.5 hrs	21 mins	2.2 hrs

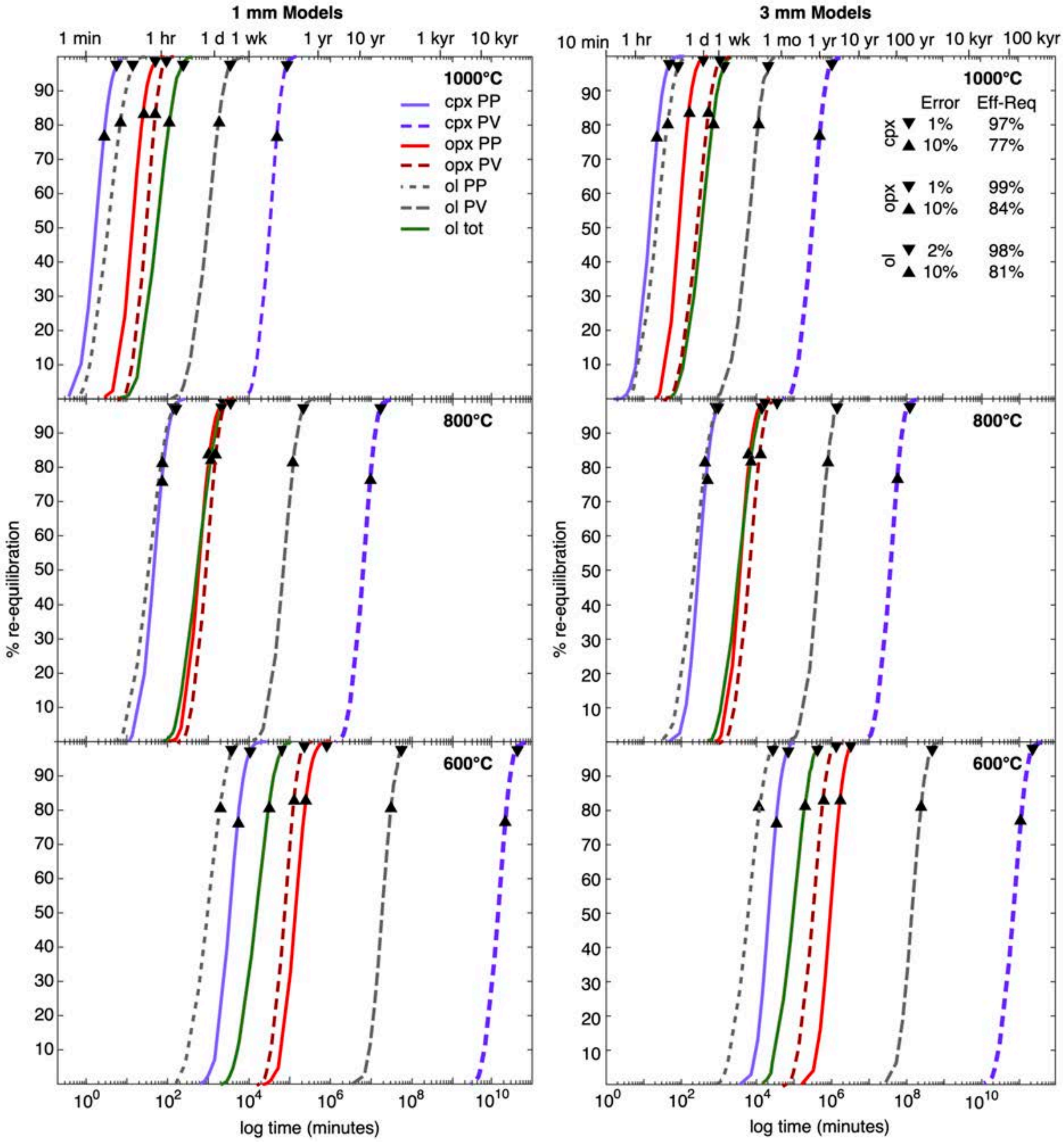

Figure S3: Detailed results of 600-1000°C models for 1-3 mm grain sizes. Each line represents the re-equilibration of the ideal core composition through time for an individual diffusion model. Clinopyroxene polaron results are shown as a solid purple line whereas vacancy results are a darker purple dashed line. Orthopyroxene polaron results are the red solid line and vacancy results are the maroon dashed line. Olivine results are as follows: total (tot) in green, olivine proton-polaron (PP) as short dashed grey lines, and olivine proton-vacancy (PV) as long dashed grey lines. Modeled timescales are plotted in log time (minutes) with conversions to common time units at the top of the figure. Black upward pointing triangles (10% analytical error) and downward pointing triangles (1% or 2% analytical error) indicate the effective %re-equilibration point for each phase, where any zonation beyond that value would be difficult to resolve outside of analytical error.

References

Ardia, P., Hirschmann, M.M., Withers, A.C., and Tenner, T.J. (2012) H_2O storage capacity of olivine at 5-8 GPa and consequences for dehydration partial melting of the upper mantle. Earth and Planetary Science Letters, 345-348. http://dx.doi.org/10.1016/j.epsl.2012.05.038

Aubaud, C., Bureau, H., Raepsaet, C., Khodja, H., Withers, A.C., Hirschmann, M.M., and Bell, D.R. (2009) Calibration of the infrared molar absorption coefficients for H in olivine, clinopyroxene, and rhyolitic glass by elastic recoil detection analysis. Chemical Geology, 262, 78-86. https://doi.org/10.1016/j.chemgeo.2009.01.001

Aubaud, C., Withers, A.C., Hirschmann, M.H., Guan, Y., Leshin, L.A., Mackwell, S.J., and Bell, D.R. (2007) Intercalibration of FTIR and SIMS for hydrogen measurements in glasses and nominally anhydrous minerals. American Mineralogist, 92, 811-828. https://doi.org/10.2138/am.2007.2248

Bali, E., Bolfan-Casanova, N., and Koga, K.T. (2008) Pressure and temperature dependence of H solubility in forsterite: An implication to water activity in the Earth interior. Earth and Planetary Science Leters, 268, 354-363. https://doi.org/10.1016/j.epsl.2008.01.035

Bell, D.R., Rossman, G.R., Maldener, J., Endisch, D., and Rauch, F. (2003) Hydroxide in olivine: A quantitative determination of the absolute amount and calibration of the IR spectrum. Journal of Geophysical Research: Solid Earth, 108, B2. https://doi.org/10.1029/2001JB000679

Bromiley, G.D., Keppler, H., McCammon, C., Bromiley, F.A., and Jacobsen, S.D. (2004) Hydrogen solubility and speciation in natural, gem-quality chromian diopside. American Mineralogist, 89, 941-949. https://doi.org/10.2138/am-2004-0703

Crank, J. (1975) The Mathematics of Diffusion, 2nd ed.: Oxford Science Publications, Oxford, 415 p.

Demouchy, S., and Bolfan-Casanova, N. (2016) Distribution and transport of hydrogen in the lithospheric mantle: A review. Lithos, 240-243, 402-425. doi: 10.1016/j.lithos.2015.11.012

Ferot, A., and Bolfan-Casanova, N. (2012) Water storage capacity in olivine and pyroxene to 14 GPa: Implications for the water content of the Earth's upper mantle and nature of seismic discontinuities. Earth and Planetary Science Letters, 349-350, 218-230. https://doi.org/10.1016/j.epsl.2012.06.022

Ferriss, E., Plank, T., and Walker, D. (2016) Site-specific hydrogen diffusion rates during clinopyroxene dehydration. Contributions to Mineralogy and Petrology, 171, 55. https://doi.org/10.1007/s00410-016-1262-8

Gose, J., Schmädicke, E., and Stalder, R. (2011) Water in mantle orthopyroxene – no visible change in defect water during serpentinization. European Journal of Mineralogy, 23, 529-536. https://doi.org/10.1127/0935-1221/2011/0023-2122

Gose, J., Schmädicke, E., and Beran, A. (2009) Water in enstatite from Mid-Atlantic Ridge peridotite: Evidence for the water content of suboceanic mantle? Geology, 37, 543-546. https://doi.org/10.1130/G25558A.1

Hauri, E., Wang, J., Dixon, J.E., King, P.L., Mandeville, C., and Newman, S. (2002) SIMS analysis of volatiles in silicate glasses 1. Calibration, matrix effects and comparisons with FTIR. Chemical Geology, 183, 99-114. https://doi.org/10.1016/S00009-2541(01)00375-8

Hirschmann, M.M., Aubaud, C., and Withers, A.C. (2005) Storage capacity of H_2O in nominally anhydrous minerals in the upper mantle. Earth and Planetary Science Letters, 236, 167-181. https://doi.org/10.1016/j.epsl.2005.04.022

Jollands, M.C., and Müntener, O. (2019) Testing orthopyroxene diffusion chronometry on rocks from the Lanzo massif (Italian Alps). Journal of Geophysical Research: Solid Earth, 124. https://doi.org/10.1029/2018JB016963

Keppler, H., and Bolfan-Casanova, N. (2006) Thermodynamics of water solubility and partitioning. Reviews in Mineralogy and Geochemistry, 62, 193-230. https://doi.org/10.2138/rmg.2006.62.9

Kohlstedt, D.L., Keppler, H., and Rubie, D.C. (1996) Solubility of water in the alpha, beta, and gamma phases of (Mg,Fe)2SiO4. Contributions to Mineralogy and Petrology, 123, 345-357. doi: 10.1007/s004100050161

Krimer, D., and Costa, F. (2017) Evaluation of the effects of 3D diffusion, crystal geometry, and initial conditions on retrieved time-scales from Fe-Mg zoning in natural oriented orthopyroxene crystals. Geochimica et Cosmochimica Acta, 196, 271-288. https://doi.org/10.1016/j.gca.2016.09.037

Kumamoto, K.M., Warren, J.M., and Hauri, E.H. (2019) Evolution of the Josephine Peridotite shear zones: Part I: Compositional variation and shear initiation. Geochemistry Geophysics Geosystems, 20. https://doi.org/.1029/2019GC008399

Kumamoto, K.M., Warren, J.M., and Hauri, E.H. (2017) New SIMS reference materials for measuring water in upper mantle minerals. American Mineralogist, 102, 537-547. https://doi.org/10.2138/am-2017-5863CCBYNCND

Le Voyer, M., Cottrell, E., Kelley, K.A., Brounce, M., and Hauri, E.H. (2015) The effect of primary vs. secondary processes on the volatile content of MORB glasses: An example from the equatorial Mid-Atlantic Ridge (5°N-3°S). Journal of Geophysical Research: Solid Earth, 120, 125-144. https://doi.org/10.1002/2014JB011160

Li, W., Jin, Z., Li, H., and Tao, C. (2017) High water content in primitive mid-ocean ridge basalt from Southwest Indian Ridge (51.56°E): Implications for recycled hydrous component in the mantle. Journal of Earth Science, 28, 411-421. https://doi.org/10.1007/s12583-017-0731-y

Ligi, M., Bonatti, E., Cipriani, A., and Ottolini, L. (2005) Water-rich basalts at mid-ocean ridge cold spots. Nature, 434, 66-69. https://doi.org/10.1038/nature03264

Longpré, M-A., Klügel, A., Diehl, A., and Stix, J. (2014) Mixing in mantle magma reservoirs prior to and during the 2011-2012 eruption at El Hierro, Canary Islands. Geology, 42, 315-318. https://doi.org/10.1130/G35165.1

Lynn, K.J., Shea, T., and Garcia, M.O. (2017) Nickel variability in Hawaiian olivine: Evaluating the relative contributions from mantle and crustal processes. American Mineralogist, 102, 507-518. https://doi.org/10.2138/am-2017-5763.

Mierdel, K., and Keppler, H. (2004) The temperature dependence of water solubility in enstatite. Contributions to Mineralogy and Petrology, 148, 305-311. https://doi.org/10.1007/s00410-004-0605-z

Mosenfelder, J.L., and Rossman, G.R. (2013a) Analysis of hydrogen and fluorine in pyroxenes I: Orthopyroxene. American Mineralogist, 95, 1026-1041. https://doi.org/10.2138/am.2013.4291

Mosenfelder, J.L., and Rossman, G.R. (2013b) Analysis of hydrogen and fluorine in pyroxenes II: Clinpyroxene. American Mineralogist, 98, 1042-1054. https://doi.org/10.2138/am.2013.4413

Mutch, E.J.F., Maclennan, J., Holland, T.J.B., and Buisman, I. (2019) Millennial storage of near-Moho magma. Science, 356, 260-264. https://doi.org/10.1126/science.aax4092

Pan, Y., and Batiza, R. (2002) Mid-ocean ridge magma chamber processes: Constraints from olivine zonation in lavas from the East Pacific Rise at 9°30'N and 10°30'N. Journal of Geophysical Research, 107, 2022. https://doi.org/10.1029/2001JB000435.

Peslier, A.H. (2010) A review of water contents of nominally anhydrous natural minerals in the mantles of Earth, Mars, and the Moon. Journal of Volcanology and Geothermal Research, 197, 239-258. https://doi.org/10.1016/j.jvolgeores.2009.10.006

Rauch, M., and Keppler, H. (2002) Water solubility in orthopyroxene. Contributions to Mineralogy and Petrology, 143, 525-536. https://doi.org/10.1007/00410-002-0355-6

Schmädicke, E., Gose, J., and Will, T.M. (2011) Heterogeneous mantle underneath the North Atlantic: Evidence from water in orthopyroxene, mineral composition and equilibrium conditions of spinel peridotite from different locations at the Mid-Atlantic Ridge. Lithos, 125, 308-320. https://doi.org/10.1016/j.lithos.2011.02.014

Shea, T., Lynn, K.J., and Garcia, M.O. (2015a) Cracking the olivine zoning code: Distinguishing between crystal growth and diffusion. Geology, 43, 935-938. https://doi.org/10.1130/G37082.1

Shea, T., Costa, F., Krimer, D., and Hammer, J.E. (2015b) Accuracy of timescales retrieved from diffusion modeling in olivine: A 3D perspective. American Mineralogist, 100, 2026-2042. https://doi.org/10.2138/am-2015-5163

Stalder, R., and Skogby, H. (2002) Hydrogen incorporation in enstatite: European Journal of Mineralogy, 14, 1139-1144. https://doi.org/10.1127/0935-1221/2002/0014-1139

Stalder, R., and Skogby, H. (2003) Hydrogen diffusion in natural and synthetic orthopyroxene: Physics and Chemistry of Minerals, 30, 12-19. https://doi.org/10.1007/s00269-002-0285-z

Stalder, R., Prechtel, F., and Ludwig, T. (2012) No site-specific infrared absorption coefficients for OH-defects in pure enstatite. European Journal of Mineralogy, 24, 465-470.

Tenner, T.J., Hirschmann, M.M., Withers, A.C., and Ardia, P. (2012) H_2O storage capacity of olivine and low-Ca clinopyroxene from 10 to 13 GPa: consequences for dehydration melting above the transition zone. Contributions to Mineralogy and Petrology, 163, 297-316. https://doi.org/10.1007/s00410-011-0675-7

Thoraval, C., and Demouchy, S. (2014) Numerical models of ionic diffusion in one and three dimensions: applications to dehydration of mantle olivine. Physics and Chemistry of Minerals, 41, 709-723. https://doi.org/10.1007/s00269-014-0685-x

Warren, J.M., and Hauri, E.H. (2014) Pyroxenes as tracers of mantle water variations. Journal of Geophysical Research: Solid Earth, 119, 1851-1881. https://doi.org/10.1002/2013JB010328

Withers, A.C., and Hirschmann, M.M. (2008) Influence of temperature, composition, silica activity and oxygen fugacity on the H_2O storage capacity of olivine at 8 GPa. Contributions to Mineralogy and Petrology, 156, 595-605. https://doi.org/10.1007/s00410-008-0303-3

Withers, A.C., Bureau, H., Raepsaet, C., and Hirschmann, M. (2012) Calibration of infrared spectroscopy by elastic recoil detection analysis of H in synthetic olivine. Chemical Geology, 334, 92-98. https://doi.org/10.1016/j.chemgeo.2012.10.002

Withers, A.C., Hirschmann, M.M., and Tenner, T.J. (2011) The effect of Fe on olivine H_2O storage capacity: Consequences for H_2O in the martian mantle. American Mineralogist, 96, 1039-1053. https://doi.org/10.2138/am.2011.3669

Woods, S.C., Mackwell, S., and Dyar, D. (2000) Hydrogen in Diopside: Diffusion profiles. American Mineralogist, 85, 480-487. https://doi.org/10.2138/am-2000-0409

Zhang, Y. (2010) Diffusion in minerals and melts: Theoretical background. Reviews in Mineralogy and Geochemistry, 72, 5-59. https://doi.org/10.2138/rmg.2010.72.2

Zhao, Y-H., Ginsberg, S.B., and Kohlstedt, D.L. (2004) Solubility of hydrogen in olivine: dependence on temperature and iron content. Conributions to Mineralogy and Petrology, 147, 155-161.